



Post-capture vibration suppression of spacecraft via a bio-inspired isolation system

Honghua Dai^{a,b,*}, Xingjian Jing^{b,*}, Yu Wang^b, Xiaokui Yue^a, Jianping Yuan^a

^a College of Astronautics, Northwestern Polytechnical University, Xi'an, China

^b Department of Mechanical Engineering, The Hong Kong Polytechnic University, Hong Kong, China

ARTICLE INFO

Article history:

Received 3 November 2017

Received in revised form 8 December 2017

Accepted 9 December 2017

Available online 22 December 2017

Keywords:

Bio-inspired

Vibration isolation

On-orbit capture

Impulsive force

Under-constrained system

Nonlinear damping

ABSTRACT

Inspired by the smooth motions of a running kangaroo, a bio-inspired quadrilateral shape (BIQS) structure is proposed to suppress the vibrations of a free-floating spacecraft subject to periodic or impulsive forces, which may be encountered during on-orbit servicing missions. In particular, the BIQS structure is installed between the satellite platform and the capture mechanism. The dynamical model of the BIQS isolation system, i.e. a BIQS structure connecting the platform and the capture mechanism at each side, is established by Lagrange's equations to simulate the post-capture dynamical responses. The BIQS system suffering an impulsive force is dealt with by means of a modified version of Lagrange's equations. Furthermore, the classical harmonic balance method is used to solve the nonlinear dynamical system subject to periodic forces, while for the case under impulsive forces the numerical integration method is adopted. Due to the weightless environment in space, the present BIQS system is essentially an under-constrained dynamical system with one of its natural frequencies being identical to zero. The effects of system parameters, such as the number of layers in BIQS, stiffness, assembly angle, rod length, damping coefficient, masses of satellite platform and capture mechanism, on the isolation performance of the present system are thoroughly investigated. In addition, comparisons between the isolation performances of the presently proposed BIQS isolator and the conventional spring-mass-damper (SMD) isolator are conducted to demonstrate the advantages of the present isolator. Numerical simulations show that the BIQS system has a much better performance than the SMD system under either periodic or impulsive forces. Overall, the present BIQS isolator offers a highly efficient passive way for vibration suppressions of free-floating spacecraft.

© 2017 Elsevier Ltd. All rights reserved.

1. Introduction

The past two decades witnessed a growing trend of on-orbit servicing (OOS) missions due to the introductions of new technologies to the design of modern satellites. It will become popular to conduct on-orbit refueling, assembly and retrieval of malfunctioning satellites in future space operations [1–4]. Besides, the removal of space debris is also becoming an urgent task [5–8], due to the increasing threat posed to the near-Earth space activities by the rapidly increasing amount of space debris.

* Corresponding authors at: Department of Mechanical Engineering, The Hong Kong Polytechnic University, Hong Kong, China.

E-mail addresses: hhdai@polyu.edu.hk (H. Dai), xingjian.jing@polyu.edu.hk (X. Jing).

For the aforementioned missions, the on-orbit capture operation plays a fundamental role. In the capture process shown in Fig. 1, the chasing satellite is expected to approach the target in a manner that at the time of collision the relative velocity between the end-effector, i.e. capture mechanism, and the target vanishes. In practice, however, there always exists an impact which results in undesirable vibration and drifting motions for the satellite platform [9], especially for capturing an uncooperative target that lacks partial state information. If the target is a satellite, its moving parts turn out to be vibration sources for the whole system after capture.

In general, post-capture vibrations of the satellite platform are primarily stimulated by two types of vibration sources, the high frequency periodic excitations and the impact excitations. The former arise from the moving payloads mounted on the target, including the reaction flywheel, the propulsor, the driving mechanism of solar panel, for which the induced vibrations are mild. A vibration experiment was conducted in China's four remote sensing satellites [10], which demonstrates that the dominate vibration sources are from reaction flywheels and radiometer, mainly distributed over 50–200 Hz with a maximum vibration acceleration being 57 mg. The latter vibration sources are due to collisions with the targets, e.g. space debris or spacecraft waiting for service [11]. No matter what kinds of excitations, the satellite platform should stay stable, otherwise the pointing accuracy and the performance of precision instruments will be damaged.

Micro-vibration control is a challenging problem in engineering, especially for spacecraft with high precision instruments whose vibration magnitude is strictly required. Although the vibration sources are not strong, micro-vibration may last for a long time because of the low damping and micro-gravity space environment [12]. In general, there are three isolation methods namely, the passive, active and semi-active control methods, among which the passive one is mostly used. A typical passive control method for vibration isolation is to use the linear spring-mass-damper (SMD) isolator. The pioneer work is attributed to Ref. [13], in which the properties of the SMD under repetitive impact were exhaustively analyzed both theoretically and experimentally. Normally, increasing the linear damping in SMD system leads to a smaller resonant amplitude, but may result in a worse isolation performance beyond the resonant range, which is a major drawback for the SMD isolator. On the other hand, the resonant frequency is expected to be smaller so that the excitation frequencies can be far away from the resonant frequency, thus leading to a weaker vibration. The resonant frequency in linear system is determined by $\sqrt{k_{eq}/m_{eq}}$, where k_{eq} and m_{eq} represent equivalent stiffness and mass respectively. However, a smaller resonant frequency implies a smaller system stiffness k_{eq} or a larger mass m_{eq} , which are corresponding to unwanted lower loading capacity or heavier satellite. To conquer these limitations, the quasi-zero-stiffness (QZS) isolator is proposed in Ref. [14], which can realize ultra-low stiffness, zero stiffness, or negative stiffness via carefully choosing structural parameters. The QZS isolator shows a better performance than the traditional SMD isolator in the vicinity of the equilibrium point due to its quasi-zero stiffness property. A variety of studies are carried out to the applications of the QZS [15–21]. However, it is reported that very complex nonlinear behaviors such as bifurcation and chaos may occur due to strong nonlinear stiffness [22,23]. Moreover, the QZS is prone to instability and low loading capability at equilibrium in case of negative stiffness [24].

In order to obtain an efficient isolation performance, a series of active vibration control methods are proposed which can achieve excellent performance for low frequency vibration, and simultaneously with sufficient loading capacity and robustness. Thayer et al. [25] designed several active control Stewart platforms using very soft axial stiffness, and a 20–25 dB vibration reduction performance was achieved in all six degrees of freedom over the bandwidth 5–20 Hz. Anderson et al. [26] studied a piezoelectric-based active vibration isolation control method for pico-satellite. Ground experiments show that effect of small vibrations on spacecraft instrument effectiveness can be significantly reduced. Wei and coauthors proposed a novel adaptive model-free active control method, which is capable of handling uncertain large-scale nonlinear systems [27–29]. Nevertheless, the need for including sensors and actuators in active controls significantly increases the system size, weight, and complexity, and therefore increases cost and potential failures. The semi-active method can be treated as a compromise between the passive and active methods. Semi-active techniques using electro-rheological fluids [30], magnetorheological fluids [31], and some smart materials [32] have been extensively investigated. Although effective, the semi-active method has a complicated structure as well.

In the past five years, the passive nonlinear vibration control method has regained a growing attention due to its high reliability, easy implementation and low cost. A scissor-like structure (SLS) or later referred to as X-shaped structure, which exploits the benefits of nonlinear damping and nonlinear stiffness induced by geometrical relationships of the rods, rotation joints and springs, was proposed and further developed by Jing and his coworkers [18,33–38]. It is demonstrated that the SLS isolator can overcome major disadvantages of the traditional SMD, the QZS and the active control vibration isolators. The SLS system can achieve better nonlinear vibration isolation using pure linear spring and damper elements. Besides, its nonlinear damping and stiffness can be flexibly designed by changing system parameters. In all existing studies of SLS isolators, however, the isolation systems are properly constrained, and the vibration sources are given base excitations. For suppressing the micro-vibrations of the free-floating spacecraft, it is necessary to set up a new isolation system which can deal with various external forces.

Biological structures enjoy excellent efficiency benefiting from millions of years of biological evolution, thus it is a wise way to learn concepts from nature [39]. Kangaroos are the only large animals to use hopping to travel. They can jump 9 m far in a single leap, with a maximum hopping speed up to 70 km/h. One of the reasons for this fast and smooth way of travel is attributed to their legs that can efficiently absorb strong impacts resulting from collisions with ground. Inspired by the smooth motion of a running kangaroo, a quadrilateral shape structure is designed in Fig. 2(b) as a basic unit for constructing the bio-inspired quadrilateral shape (BIQS) isolation system in Fig. 3. The quadrilateral shape structure is one kind of the

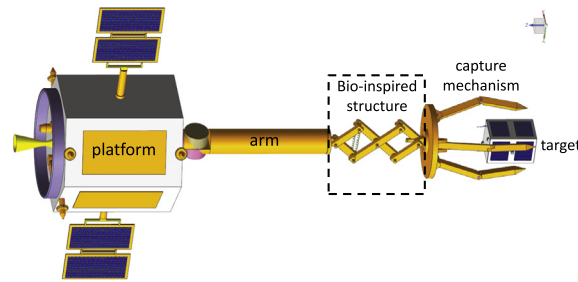


Fig. 1. Schematic diagram of an on-orbit capture mission, i.e. a chasing satellite moves axially to capture a untumbling space target which may be debris or a nano-satellite. The BIQS structure is installed between the arm and the capture mechanism to suppress vibrations.

limb-like or X-shaped structure studied in Ref. [35]. Specifically, the two rods plotted in solid lines in Fig. 2(b) imitate the kangaroo's leg bones. In addition, two additional rods (plotted in dotted lines) and a spring are added for the purpose of imitating the functions of the tendons and muscles. The collision with the ground at the time of falling down is represented by an impulsive force, and the main upper body is represented by a mass denoted by "body".

Based on the proposed bio-inspired unit structure in Fig. 2(b), a BIQS isolation system is proposed to simulate the vibrations of the floating spacecraft. The BIQS system is essentially an under-constrained two degree-of-freedom (DOF) system, in which an n unit structures (or named n layers) are used to connect m_1 and m_2 , where m_1 and m_2 are the total masses to the left and right of the bio-inspired structure in Fig. 1, respectively. For the sake of brevity, m_1 and m_2 are interchangeable with satellite platform and capture mechanism hereafter. The dynamical model is established in Lagrangian formulations for the case under periodic excitation, which can be solved accurately by the harmonic balance method [40,41]. Once the free-floating spacecraft is subject to impulsive force, a modified version of Lagrange's equations has to be derived. Under this circumstance the response is no longer periodic, therefore the numerical integration method is employed. The isolation performance of the proposed BIQS system is verified via comparing with the classical spring-mass-damper (SMD) isolation system. For reasonable comparisons, the stiffness and damping coefficient of the SMD are set to be the same as that of the linearized counterpart to the BIQS system. Numerical simulations demonstrate that the BIQS system shows a much better isolation performance. Furthermore, the effect of the nonlinear damping is also investigated, demonstrating that the nonlinear damping has an effect of suppressing vibrations in high frequency region. Overall, the main contributions of this paper are threefold: (i) the BIQS isolation system is first proposed to simulate the vibrations of an under-constrained free-floating spacecraft; (ii) different from existing studies where the external excitations are base type excitations, the external excitations considered in this study are periodic and impulsive forces so as to simulate the vibration sources on-board the satellite; (iii) a modified version of Lagrange's equations has been derived to handle the modeling of the BIQS system under an impact.

The rest of this paper is organized as follows. The equations of motion of the present BIQS isolation system are established in Section 2. Section 3 introduces the harmonic balance (HB) method and an efficient nonlinear algebraic equation solver for solving the periodic solutions to the BIQS system. In Section 4, properties of the natural frequency and nonlinear damping of the BIQS are investigated. The accuracy of the HB method is verified by the benchmark fourth-order Runge-Kutta (RK4) method. More importantly, the isolation performance of the BIQS system is evaluated in numerical simulations, and the effects of system parameters on the isolation performance are thoroughly investigated. Finally, conclusions are drawn in Section 5.

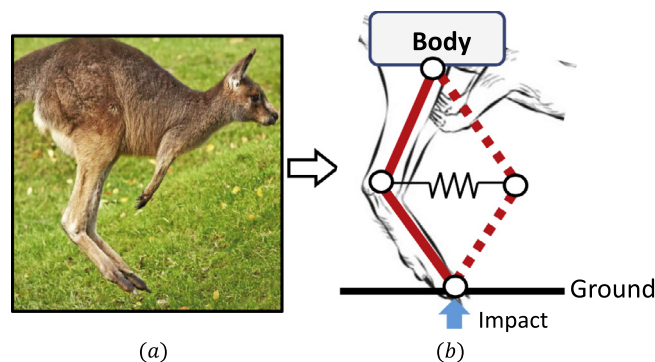


Fig. 2. (a) A jumping kangaroo and (b) the bio-inspired quadrilateral shape structure.

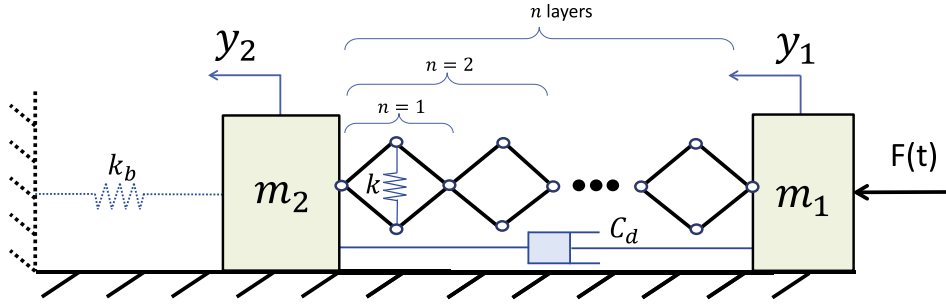


Fig. 3. Schematic diagram of an n -layer bio-inspired quadrilateral shape (BIQS) isolation system. Note that m_1 represents the mass of the capture mechanism plus the target; m_2 is the mass of the satellite platform plus the arm; spring k_b is used for simplicity of modeling, and is set to zero in simulations. Air drag and ground friction do not exist.

2. Formulation of equations of motion

2.1. Geometrical relations

Shown in Fig. 4 is the geometrical relation between the initial and the deformed states for the basic unit structure. The configurations for the initial and deformed states are plotted in solid and dotted lines, respectively. Since the present dynamical system is a two degree-of-freedom (DOF) system, two coordinates y_1 and y_2 representing the displacements of m_1 and m_2 are chosen as the generalized coordinates with the positive directions pointing to the left, see Fig. 3. Two more constrained coordinates x and ϕ are employed in the dynamical modeling as shown in Fig. 4, where x is the vertical displacement of the connecting joint A and ϕ is the angle of rotation of the rod OA. $h = (y_2 - y_1)/2n$ is the horizontal displacement of point A, which is used in constructing the geometric relations. l and θ_0 are the length of the rods and the initial assembly angle, respectively. The positive directions for them are defined in figure.

Once the generalized coordinates y_1 and y_2 are prescribed, the intermediate coordinates x and ϕ can be uniquely determined. According to the horizontal and vertical movements of A, it can be obtained that

$$l \sin \theta_0 - \frac{y_1 - y_2}{2n} = l \sin(\theta_0 - \phi),$$

$$l \cos \theta_0 + x = l \cos(\theta_0 - \phi).$$

The constrained coordinates x and ϕ are not independent, and should be expressed by the generalized coordinates as:

$$x = \sqrt{l^2 - \left(l \sin \theta_0 - \frac{y_1 - y_2}{2n}\right)^2} - l \cos \theta_0, \quad (1)$$

$$\phi = \theta_0 - \arctan \left(\frac{l \sin \theta_0 - \frac{y_1 - y_2}{2n}}{\sqrt{l^2 - \left(l \sin \theta_0 - \frac{y_1 - y_2}{2n}\right)^2}} \right). \quad (2)$$

Obviously, x and ϕ have a nonlinear relation with the generalized coordinates, and the rotation angle ϕ is restricted such that $\theta_0 - 90^\circ < \phi < \theta_0$. In fact, the nonlinear geometrical relations are responsible for the presence of nonlinear damping and nonlinear stiffness in the BIQS system, in which only pure linear damper and spring elements are used.

2.2. Lagrange's equations

Lagrange's equations are used to formulate the nonlinear dynamical system. The spring k_b is retained in the modeling, and later removed, i.e. set $k_b = 0$, to simulate the free-floating environment in space. The kinetic energy, the potential energy and the virtual work done by nonconservative forces should be expressed first. The kinetic energy for the BIQS system in Fig. 3 is

$$T = \frac{1}{2} m_1 \dot{y}_1^2 + \frac{1}{2} m_2 \dot{y}_2^2. \quad (3)$$

Note that the masses of the rods and the joints are neglected because they are much lighter than m_1 and m_2 . The potential energy can be written as

$$V = \frac{1}{2} k(x_0 + 2x)^2 + \frac{1}{2} k_b(x_b + y_2)^2 \quad (4)$$

where x_0 and x_b are the elongation of spring k and compression of spring k_b in the initial state, respectively. If the initial state is chosen such that the two springs are untensioned, then $x_0 = 0$ and $x_b = 0$. The virtual work done by nonconservative forces is

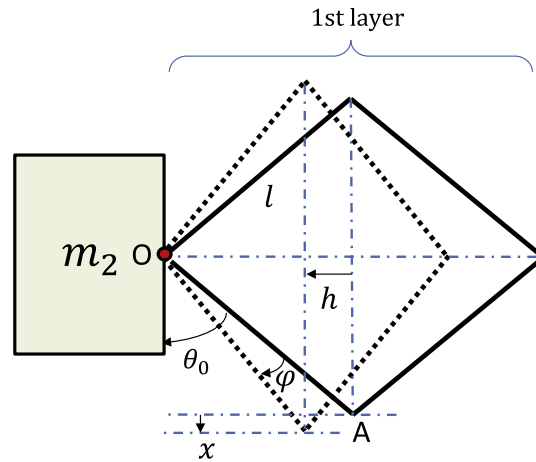


Fig. 4. The geometric relationship between the initial and deformed configurations.

$$\delta W_n = -2n_x c \dot{\phi} \delta \phi + C_d (\dot{y}_2 - \dot{y}_1) \delta y_1 - C_d (\dot{y}_2 - \dot{y}_1) \delta y_2 + F(t) \delta y_1, \quad (5)$$

where $n_x = 3n + 1$ stands for the number of joints in each layer, and c , C_d are the rotation friction and damping coefficients, respectively. It is noted that the first term on the right side of the above equation account for the virtual work done by friction force of the rotation joints, and the second and third terms are for the damping force. Since the present system is determined by two generalized coordinates, thus

$$\delta W_n \stackrel{\text{def}}{=} Q_1 \delta y_1 + Q_2 \delta y_2, \quad (6)$$

in which $Q_i = 0 (i = 1, 2)$ are the generalized forces arising from nonconservative forces.

Comparing Eqs. (5) and (6), we have

$$Q_1 = -2n_x c \dot{\phi} \frac{\partial \phi}{\partial y_1} + C_d (\dot{y}_2 - \dot{y}_1) + F(t), \quad (7)$$

$$Q_2 = -2n_x c \dot{\phi} \frac{\partial \phi}{\partial y_2} + C_d (\dot{y}_1 - \dot{y}_2). \quad (8)$$

The equations of motion of the present system under external forces can be established by Lagrange's equations:

$$\frac{d}{dt} \left(\frac{\partial L}{\partial \dot{y}_i} \right) - \frac{\partial L}{\partial y_i} = Q_i, \quad i = 1, 2, \quad (9)$$

where $L = T - V$ is referred to as the Lagrangian. Concretely speaking, the nonconservative forces comprise the external force $F(t)$, the damping force and the friction force of rotating joints.

Substituting Eqs. (3), (4), (7) and (8) into the Lagrange's equations yields

$$m_1 \ddot{y}_1 + 2k(x_0 + 2x) \frac{\partial x}{\partial y_1} + 2n_x c \dot{\phi} \frac{\partial \phi}{\partial y_1} + C_d (\dot{y}_1 - \dot{y}_2) = F(t), \quad (10)$$

$$m_2 \ddot{y}_2 + 2k(x_0 + 2x) \frac{\partial x}{\partial y_2} + k_b(x_b + y_2) + 2n_x c \dot{\phi} \frac{\partial \phi}{\partial y_2} + C_d (\dot{y}_2 - \dot{y}_1) = 0. \quad (11)$$

The constrained coordinates should be replaced by the generalized coordinates in the above equations. According to Eqs. (1) and (2), the involved quantities above can be expressed in terms of y_1 and y_2 as follows

$$\begin{cases} \frac{\partial x}{\partial y_1} = \frac{l \sin \theta_0 - \frac{y_1 - y_2}{2n}}{2n \sqrt{l^2 - \left(l \sin \theta_0 - \frac{y_1 - y_2}{2n} \right)^2}}, \\ \frac{\partial x}{\partial y_2} = -\frac{l \sin \theta_0 - \frac{y_1 - y_2}{2n}}{2n \sqrt{l^2 - \left(l \sin \theta_0 - \frac{y_1 - y_2}{2n} \right)^2}}, \\ \dot{\phi} = \frac{\dot{y}_1 - \dot{y}_2}{2n \sqrt{l^2 - \left(l \sin \theta_0 - \frac{y_1 - y_2}{2n} \right)^2}}, \\ \frac{\partial \phi}{\partial y_1} = \frac{1}{2n \sqrt{l^2 - \left(l \sin \theta_0 - \frac{y_1 - y_2}{2n} \right)^2}}, \\ \frac{\partial \phi}{\partial y_2} = -\frac{1}{2n \sqrt{l^2 - \left(l \sin \theta_0 - \frac{y_1 - y_2}{2n} \right)^2}}. \end{cases} \quad (12)$$

In the following numerical examples, the initial state is chosen such that the two springs are undeformed, i.e. $x_0 = 0$, $x_b = 0$. Since this paper is focused on the simulation of the vibration isolations of free-floating spacecraft, so the spring connecting the base and the satellite platform is removed, i.e. $k_b = 0$. Using these conditions and substituting Eqs. (12) into Eqs. (10), (11) yields

$$m_1 \ddot{y}_1 + \left\{ \frac{n_x c}{2n^2 \left[l^2 - \left(l \sin \theta_0 - \frac{y_1 - y_2}{2n} \right)^2 \right]} + C_d \right\} (\dot{y}_1 - \dot{y}_2) - \frac{k}{n^2} (y_1 - y_2) - \frac{2kl \cos \theta_0}{n} \frac{l \sin \theta_0 - \frac{y_1 - y_2}{2n}}{\sqrt{l^2 - \left(l \sin \theta_0 - \frac{y_1 - y_2}{2n} \right)^2}} + \frac{2kl \sin \theta_0}{n} = F(t) \quad (13)$$

$$m_2 \ddot{y}_2 - \left\{ \frac{n_x c}{2n^2 \left[l^2 - \left(l \sin \theta_0 - \frac{y_1 - y_2}{2n} \right)^2 \right]} + C_d \right\} (\dot{y}_1 - \dot{y}_2) + \frac{k}{n^2} (y_1 - y_2) + \frac{2kl \cos \theta_0}{n} \frac{l \sin \theta_0 - \frac{y_1 - y_2}{2n}}{\sqrt{l^2 - \left(l \sin \theta_0 - \frac{y_1 - y_2}{2n} \right)^2}} - \frac{2kl \sin \theta_0}{n} = 0. \quad (14)$$

Eqs. (13) and (14) are the equations of motion of the BIQS isolation system under an external force $F(t)$.

2.3. Lagrange's equations for impulsive force

In case that the capture mechanism m_1 undergoes impulsive forces, the standard Lagrange's equations need to be modified. The Lagrange's equations are

$$\frac{d}{dt} \left(\frac{\partial L}{\partial \dot{y}_i} \right) - \frac{\partial L}{\partial y_i} = \hat{F}_i(t), \quad i = 1, 2, \dots, n \quad (15)$$

where $\hat{F}_i(t)$, $t \in [0, \Delta t]$ are impulsive forces, i.e. Δt is infinitesimal and $\int_0^{\Delta t} \hat{F}_i(t) dt$ are constant quantities. In this case, the vibration of the BIQS system is due to collisions with space debris or malfunctioning satellites. Multiplying dt for both sides of Eq. (15), and integrating over t from 0 to Δt , yields

$$\int_0^{\Delta t} d \left(\frac{\partial L}{\partial \dot{y}_i} \right) - \int_0^{\Delta t} \frac{\partial L}{\partial y_i} dt = \int_0^{\Delta t} \hat{F}_i dt. \quad (16)$$

Since $\partial L / \partial y_i$ is a finite quantity in $t \in [0, \Delta t]$, we can always find a constant M such that $|\partial L / \partial y_i| < M$. According to Lagrange mean value theorem, $\int_0^{\Delta t} \partial L / \partial y_i dt < M \Delta t$. Because Δt is infinitesimal the second term in the above equation vanishes. Therefore, Eq. (16) degenerates to

$$\frac{\partial L}{\partial \dot{y}_i} \Big|_0^{\Delta t} = I_i \quad (17)$$

where $I_i \stackrel{\text{def}}{=} \int_0^{\Delta t} \hat{F}_i dt$ are generalized momenta. Because the impulsive forces act on the system during a negligibly small period, generalized momenta I_i are equal to and thus can be referred to as generalized impulses. Eq. (17) can be used to calculate the instantaneous velocities of the dynamical system after impact. Essentially, the effect of the impulses acting on the system can be converted into the system's initial states. Since the acting time of the impulsive force is infinitesimal, i.e., $\Delta t \rightarrow 0$, the starting time instant after impact can be marked as $t_{\text{start}} = 0^+$.

3. Solution methods

It is emphasized that in case of impulsive forces the dynamical responses are not periodic. Therefore, the RK4 method is employed to numerically integrate the governing equations. In using the RK4, the governing Eqs. (13) and (14) should be written in the form of first order differential equations:

$$\begin{cases} \dot{y}_1 = y_3, \\ \dot{y}_2 = y_4, \\ \dot{y}_3 = -\frac{1}{m_1} \left\{ \left(\frac{n_x c}{2n^2 \left[l^2 - \left(l \sin \theta_0 - \frac{y_1 - y_2}{2n} \right)^2 \right]} + C_d \right) (y_3 - y_4) - \frac{k}{n^2} (y_1 - y_2) - \frac{2kl \cos \theta_0}{n} \frac{l \sin \theta_0 - \frac{y_1 - y_2}{2n}}{\sqrt{l^2 - \left(l \sin \theta_0 - \frac{y_1 - y_2}{2n} \right)^2}} + \frac{2kl \sin \theta_0}{n} \right\}, \\ \dot{y}_4 = \frac{1}{m_2} \left\{ \left(\frac{n_x c}{2n^2 \left[l^2 - \left(l \sin \theta_0 - \frac{y_1 - y_2}{2n} \right)^2 \right]} + C_d \right) (y_3 - y_4) - \frac{k}{n^2} (y_1 - y_2) - \frac{2kl \cos \theta_0}{n} \frac{l \sin \theta_0 - \frac{y_1 - y_2}{2n}}{\sqrt{l^2 - \left(l \sin \theta_0 - \frac{y_1 - y_2}{2n} \right)^2}} + \frac{2kl \sin \theta_0}{n} \right\}. \end{cases} \quad (18)$$

In this case, the initial variable states $y|_{t=0^+}$ should be calculated from Eq. (17) to account for the impact I_i .

3.1. Nonlinear approximation via Taylor series

The amplitude-frequency responses of the BIQS system, governed by Eqs. (13) and (14), are analyzed by the HB method. In the process of using HB method, the Fourier expansion should be implemented for all terms for balancing the coefficient of each harmonic. Thus, the nonlinear terms in Eqs. (13) and (14) have to be approximated by polynomials. The two variable Taylor expansion series are adopted herein to approximate the non-polynomial functions. Firstly, let

$$\tilde{f}(y_1, y_2) = \frac{1}{l^2 - (l \sin \theta_0 - \frac{y_1 - y_2}{2n})^2}, \quad \tilde{g}(y_1, y_2) = \frac{1}{\sqrt{l^2 - (l \sin \theta_0 - \frac{y_1 - y_2}{2n})^2}}.$$

Then, expanding $\tilde{f}(y_1, y_2)$ and $\tilde{g}(y_1, y_2)$ about the initial state ($y_1 = 0, y_2 = 0$) and retaining the terms up to third order generates

$$\begin{aligned} \tilde{f}_3(y_1, y_2) &= \frac{1}{l^2} \sec^2 \theta_0 - \frac{1}{nl^3} \tan \theta_0 \sec^3 \theta_0 (y_1 - y_2) \\ &\quad + \frac{1}{4n^2 l^4} (\sec^6 \theta_0 + 3 \tan^2 \theta_0 \sec^4 \theta_0) (y_1 - y_2)^2 \\ &\quad - \frac{1}{2n^3 l^5} (\tan \theta_0 \sec^7 \theta_0 + \tan^3 \theta_0 \sec^5 \theta_0) (y_1 - y_2)^3, \\ \tilde{g}_3(y_1, y_2) &= \frac{1}{l} \sec \theta_0 - \frac{1}{2nl^2} \tan \theta_0 \sec^2 \theta_0 (y_1 - y_2) \\ &\quad + \frac{1}{8n^2 l^3} (\sec^5 \theta_0 + 2 \tan^2 \theta_0 \sec^3 \theta_0) (y_1 - y_2)^2 \\ &\quad - \frac{1}{16n^3 l^4} (3 \tan \theta_0 \sec^6 \theta_0 + 2 \tan^3 \theta_0 \sec^4 \theta_0) (y_1 - y_2)^3. \end{aligned}$$

Employing the third order Taylor expansion series, the equations of motion of the dynamical system are transformed into

$$m_1 \ddot{y}_1 + [\gamma_0 + \gamma_1(y_1 - y_2) + \gamma_2(y_1 - y_2)^2 + \gamma_3(y_1 - y_2)^3] (\dot{y}_1 - \dot{y}_2) + \alpha_1(y_1 - y_2) + \alpha_2(y_1 - y_2)^2 + \alpha_3(y_1 - y_2)^3 + \alpha_4(y_1 - y_2)^4 = F(t), \quad (19)$$

$$m_2 \ddot{y}_2 - [\gamma_0 + \gamma_1(y_1 - y_2) + \gamma_2(y_1 - y_2)^2 + \gamma_3(y_1 - y_2)^3] (\dot{y}_1 - \dot{y}_2) - \alpha_1(y_1 - y_2) - \alpha_2(y_1 - y_2)^2 - \alpha_3(y_1 - y_2)^3 - \alpha_4(y_1 - y_2)^4 = 0, \quad (20)$$

where

$$\begin{aligned} \gamma_0 &= \frac{n_x c}{2n^2 l^2} \sec^2 \theta_0 + C_d, \\ \gamma_1 &= -\frac{n_x c}{2n^3 l^3} \tan \theta_0 \sec^3 \theta_0, \\ \gamma_2 &= \frac{n_x c}{8n^4 l^4} (\sec^6 \theta_0 + 3 \tan^2 \theta_0 \sec^4 \theta_0), \\ \gamma_3 &= -\frac{n_x c}{4n^5 l^5} (\tan \theta_0 \sec^7 \theta_0 + \tan^3 \theta_0 \sec^5 \theta_0), \end{aligned}$$

and

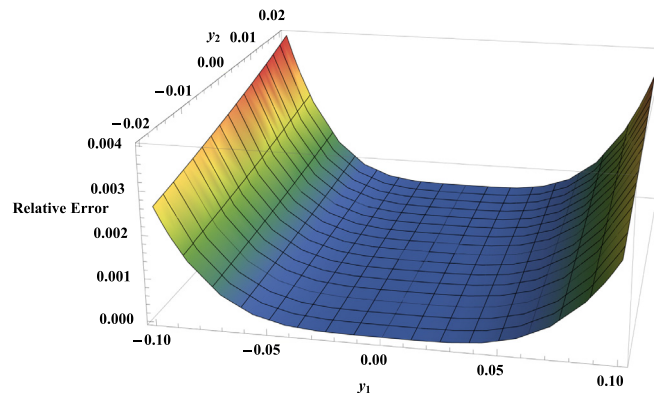


Fig. 5. The relative errors between the function $\tilde{f}(y_1, y_2)$ and its third order Taylor expansion approximation. The relative error is defined as $|\tilde{f}_3 - \tilde{f}|/\tilde{f}$.

$$\begin{aligned}\alpha_1 &= \frac{k}{n^2} (\sec^2 \theta_0 - 1), \\ \alpha_2 &= -\frac{3k}{4n^3 l} \sec^3 \theta_0 \tan \theta_0, \\ \alpha_3 &= -\frac{k}{8n^4 l^2} \sec^6 \theta_0 (2 \cos 2\theta_0 - 3), \\ \alpha_4 &= -\frac{k}{32n^5 l^3} \sec^6 \theta_0 (9 \sin \theta_0 - \sin 3\theta_0).\end{aligned}$$

The relative errors between the original nonlinear function \tilde{f} and its corresponding third order Taylor approximation \tilde{f}_3 are given in Fig. 5. In the calculation, the structural parameters are chosen to be $n = 2$, $l = 0.2$ and $\theta_0 = \pi/6$ and the comparison domain is $y_1 \in [-0.10, 0.10]$ and $y_2 \in [-0.02, 0.02]$, which is sufficient to cover the real operation range in the following numerical simulations. It can be seen that the relative error is less than 0.4% in the prescribed domain. The accuracies of the first order and second order Taylor approximations are also analyzed, whose maximum errors are 6% and 13%, respectively. In addition, the accuracy of the third order Taylor approximation of $\tilde{g}_3(y_1, y_2)$ is inspected, and the maximum relative error is less than 0.02%. In sum, using third order Taylor approximation is sufficient for the present system.

3.2. Harmonic balance method

In this study, the BIQS isolation system is investigated for two scenarios: under harmonic external force, and under impulsive force. For the former case, the periodic external force is assumed to be $F(t) = A \cos \omega t$. For the dynamical system governed by nonlinear ODEs (19) and (20), its close form exact solution is not available. We resort to HB method to calculate the approximate periodic solutions.

In using the HB method, the trial solutions are assumed as truncated Fourier expansion series

$$\begin{aligned}y_1 &= a_0 + \sum_{i=1}^N (a_{2i-1} \cos i\omega t + a_{2i} \sin i\omega t) \\ y_2 &= b_0 + \sum_{i=1}^N (b_{2i-1} \cos i\omega t + b_{2i} \sin i\omega t),\end{aligned}$$

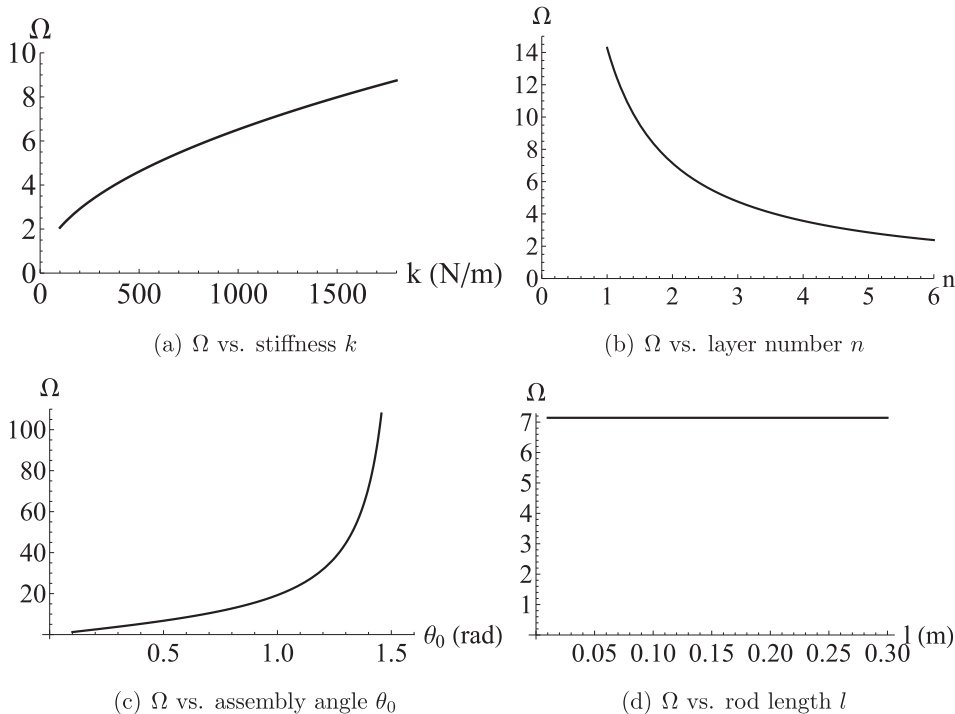


Fig. 6. The natural frequency Ω versus (a) spring stiffness k ; (b) number of layers n ; (c) assembly angle θ_0 ; (d) rod length l .

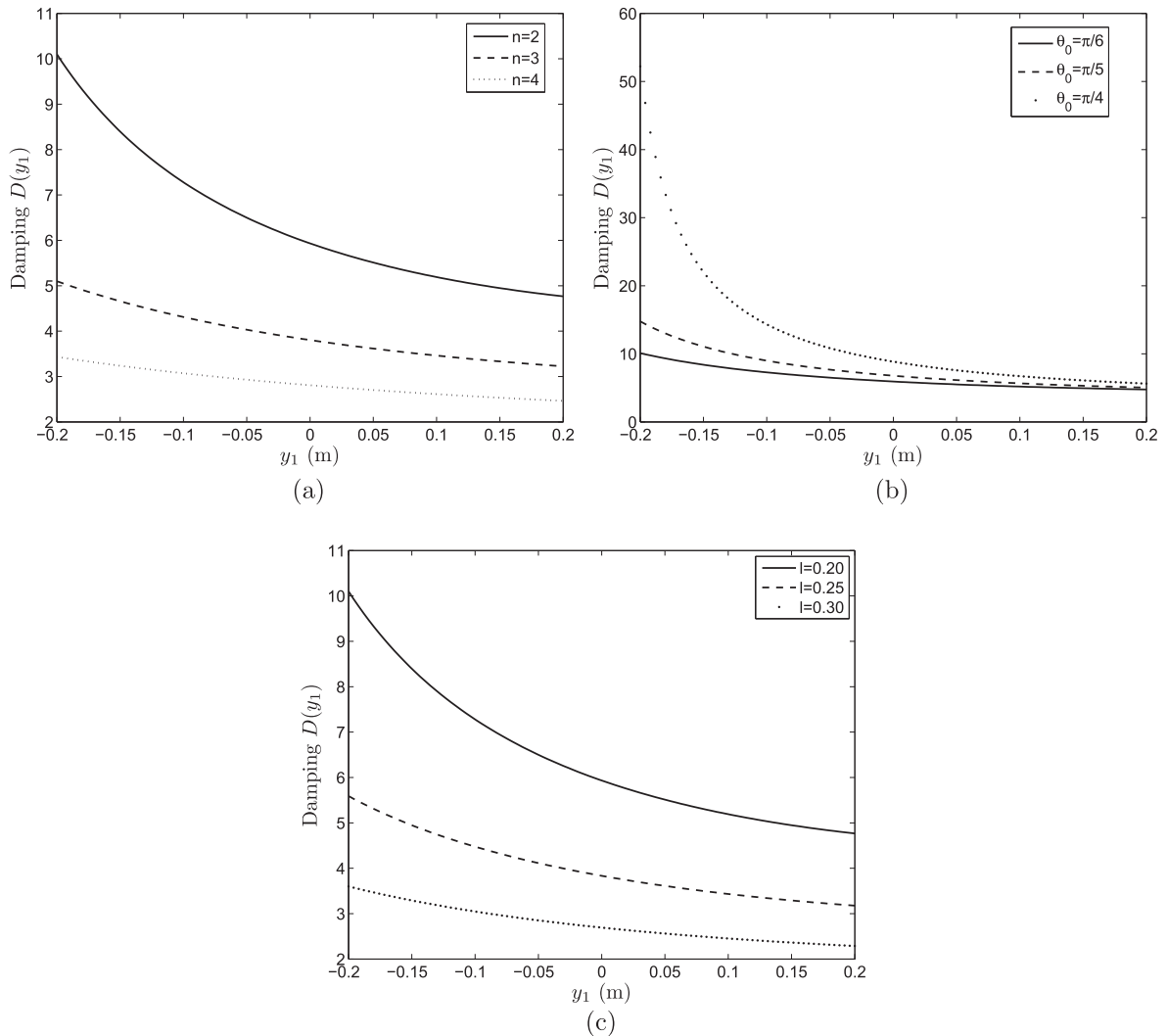


Fig. 7. Nonlinear damping $D(y_1)$ varies with displacement y_1 for different (a) number of layers; (b) assembly angles; and (c) rod lengths. Note that y_2 is set to zero in computation.

where a_i and b_i are unknown coefficients, and N is the order of the HB method. Upon substituting the trial solutions y_1 and y_2 into the governing Eqs. (19) and (20), and collecting the coefficients of each harmonic, we can obtain a system of nonlinear algebraic equations (NAEs): $F_i(a_j, b_j) = 0$, ($i = 1, \dots, 4N + 2; j = 0, \dots, 2N$) for the unknown coefficients. Let $\mathbf{x} = [a_0, a_1, \dots, a_{2N}, b_0, b_1, \dots, b_{2N}]^T$, the NAE system can be rewritten in a standard form $\mathbf{F}(\mathbf{x}) = \mathbf{0}$, which are readily solved by nonlinear iterative method, such as the Newton-Raphson method. In this study, a novel Jacobian-inversion-free method, named the optimal iterative algorithm (OIA) [42], which is more robust to initial conditions than the Newton-Raphson method, is applied to solve the NAEs.

4. Results and discussions

In the following computations, the system parameters are chosen as $m_1 = 2$ kg, $m_2 = 100$ kg, $k = 1200$ N/m, $n = 2$, $\theta_0 = \pi/6$, $l = 0.2$ m, $c = 0.2$ and $C_d = 0.1$. The parameter values given above are fixed as reference values unless otherwise specified. The SI units are used in this paper. For simplicity, the SI units are omitted in the followings.

4.1. Natural frequencies

Conventionally, there exist two natural frequencies for a standard two DOF system. The natural frequencies of a nonlinear dynamical system are commonly obtained from its linearized counterpart. In the present system, the natural frequencies $\Omega_{1,2}$ can be computed by

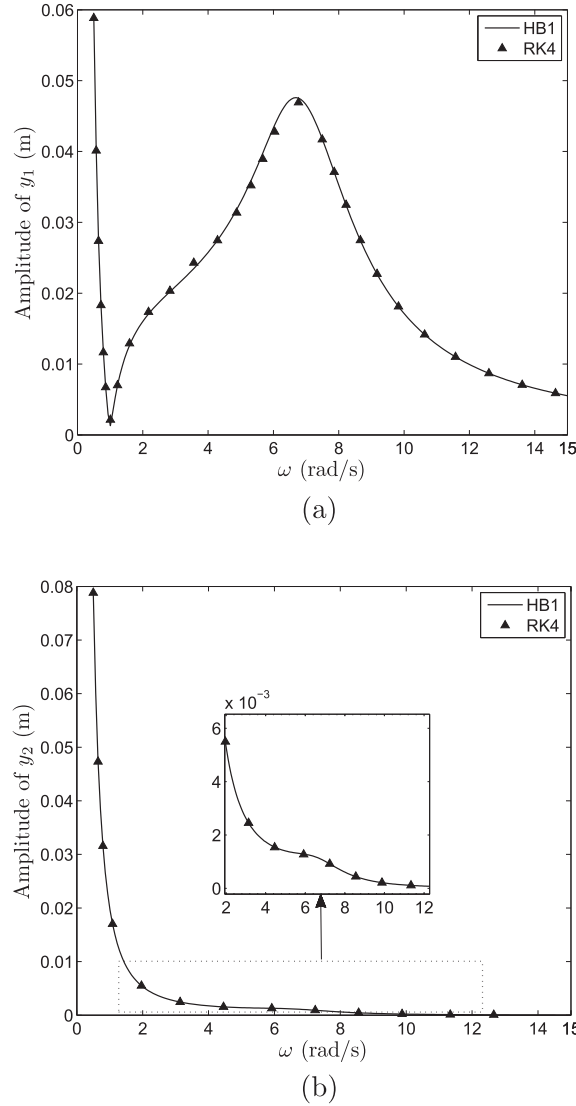


Fig. 8. Amplitudes of (a) y_1 and (b) y_2 versus excitation frequency by the RK4 and HB1 methods. The BQS system is under an external force $F = 2 \cos \omega t$, with system parameters $m_1 = 2$, $m_2 = 100$, $k = 1200$, $n = 2$, $\theta_0 = \pi/6$, $l = 0.2$, $c = 0.2$ and $C_d = 0.1$. The integration step for RK4 is $\Delta t = 0.01$, and the initial conditions are $\mathbf{y} = [0, 0, 0, 0]^T$.

$$|\mathbf{K} - \Omega^2 \mathbf{M}| = 0 \quad (21)$$

where

$$\mathbf{K} = \begin{pmatrix} \alpha_1 & -\alpha_1 \\ -\alpha_1 & \alpha_1 \end{pmatrix}, \quad \mathbf{M} = \begin{pmatrix} m_1 & 0 \\ 0 & m_2 \end{pmatrix}.$$

Solving the characteristic equation generates,

$$\Omega_1 = 0, \Omega_2 = \sqrt{\frac{\alpha_1(m_1 + m_2)}{m_1 m_2}}. \quad (22)$$

Due to the fact that the present system is under-constrained, it owns two kinds of natural frequencies. One is greater than zero and represents the oscillating mode, and the other is equal to zero corresponding to rigid body motion which means the system translates without changing shape.

Interestingly, Ω_1 is identical to zero, which means that an ultra low frequency force, $\omega \rightarrow 0$, leads to a large amplitude motion, which is consistent with intuition that a nearly constant force keeps pushing the floating system away. For the system with reference parameter values given above, the natural frequencies are $\Omega_1 = 0$ and $\Omega_2 = 7.14$. In the following analysis

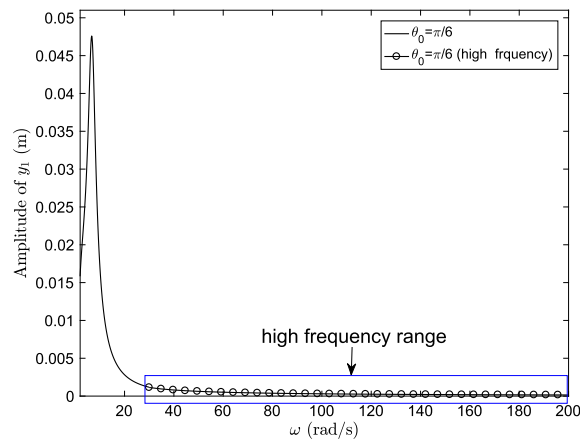


Fig. 9. Amplitude frequency response curve with a wide band of frequencies.

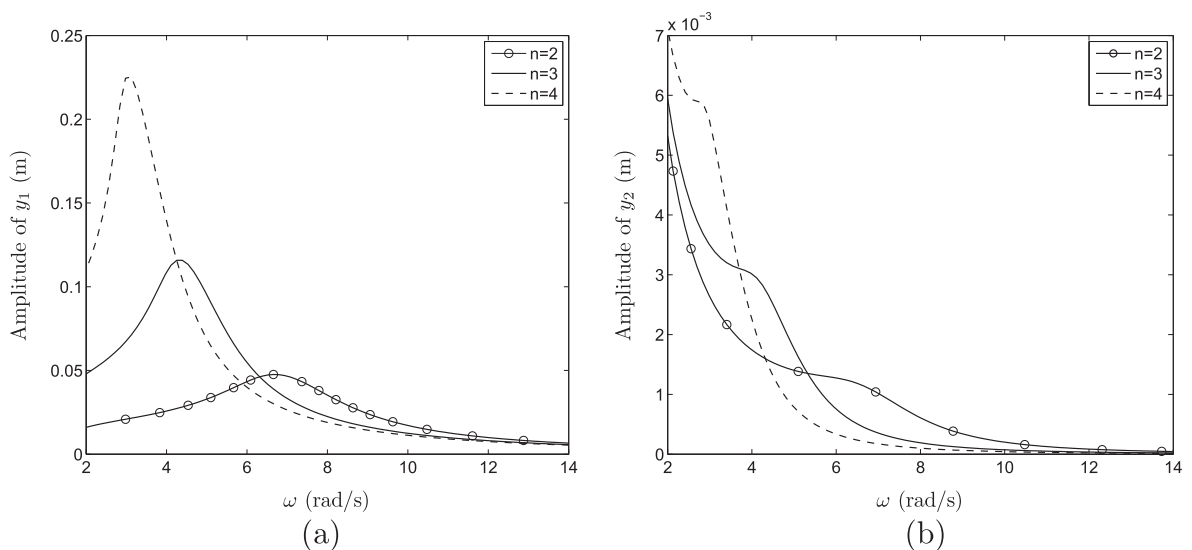


Fig. 10. (a) Amplitude of y_1 versus excitation frequency ω , (b) amplitude of y_2 versus ω for different number of layers n .

Ω_2 is denoted by Ω for brevity, and referred to as natural frequency of the system. Shown in Fig. 6 are the natural frequencies changing with structural parameters. Fig. 6(a) shows the natural frequency versus spring stiffness k , which indicates the natural frequency Ω arises with the increase of stiffness. Fig. 6(b) shows the natural frequency versus layer number, suggesting that Ω decreases with the increase of n . In general, the natural frequency of the a dynamical system is determined by $\sqrt{k_{eq}/m_{eq}}$, where k_{eq} and m_{eq} represent equivalent stiffness and mass respectively. In the present system, a larger n reduces the natural frequency (see Fig. 6(b)), which implies that multiplying the number of the layers will make the system softer, i.e. k_{eq} decreases.

Fig. 6(c) shows that Ω increases with the increase of θ_0 , indicating that a larger angle θ_0 stiffens the system. Specifically, Ω increases almost linearly with θ_0 in the region $\theta_0 \in (0, 57.3^\circ)$, beyond which Ω increases much more rapidly. Theoretically, the natural frequency Ω may approach infinity if θ_0 approaches 90° . However, this never happens in the structure design. Fig. 6(d) shows the relation between natural frequency and the rod length, which implies that Ω is independent of l . Hence, in the practical applications, the size of the rod can be designed rather freely without changing the resonant frequency.

In sum, the natural frequency is adjustable with respect to structural parameters. Reducing k , θ_0 and increasing n can decrease the resonant frequency, which would be beneficial to isolation performance.

4.2. Nonlinear damping

The nonlinear damping is a distinct property belonging to the BIQS isolator which will be verified to show a very good isolation performance. As can be seen from the governing Eqs. (13) and (14), the nonlinear damping is

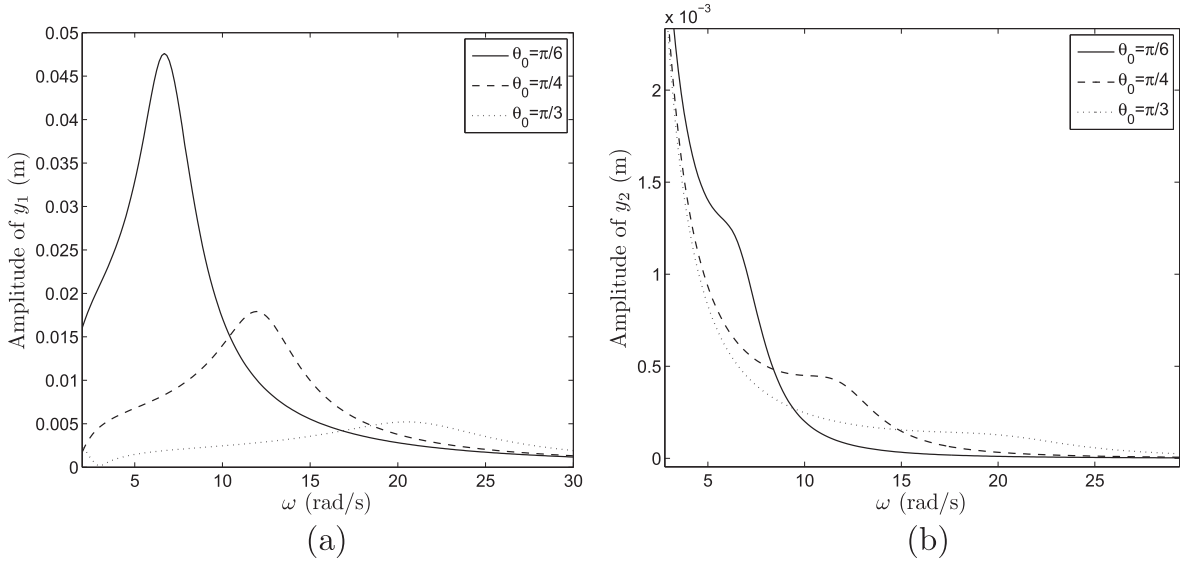


Fig. 11. Amplitudes of (a) y_1 and (b) y_2 versus excitation frequency ω for different assembly angles.

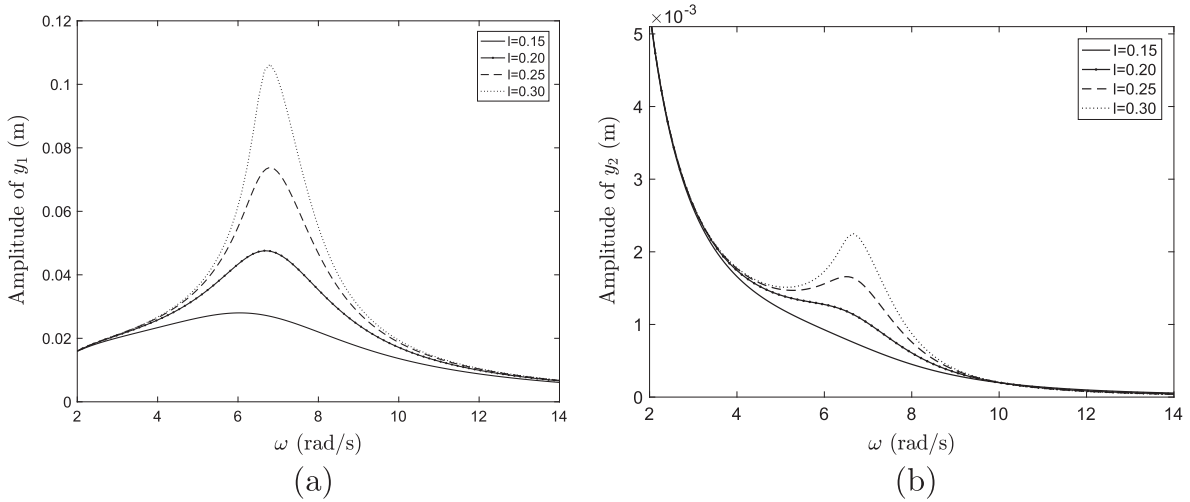


Fig. 12. Amplitudes of (a) y_1 and (b) y_2 versus excitation frequency ω for different values of rod length l .

$$D(y_1, y_2) = \frac{n_x c}{2n^2 \left[l^2 - \left(l \sin \theta_0 - \frac{y_1 - y_2}{2n} \right)^2 \right]} + C_d. \quad (23)$$

The nonlinear damping $D(y_1, y_2)$ is approximated in Eqs. (19) and (20) via the third order Taylor expansion

$$D(y_1, y_2) \approx \underbrace{\gamma_0}_{\text{linear}} + \underbrace{\gamma_1(y_1 - y_2) + \gamma_2(y_1 - y_2)^2 + \gamma_3(y_1 - y_2)^3}_{\text{nonlinear}}, \quad (24)$$

where γ_0 and the rest terms are the linear and nonlinear components respectively.

In this section, attentions are paid to the influences of structural parameters on the nonlinear damping, so that the original $D(y_1, y_2)$ in Eq. (23) is adopted. In numerical simulations for the analysis of isolation performance, the advantages of nonlinear damping over linear damping is investigated through using Eq. (24).

Fig. 7 shows the nonlinear damping $D(y_1)$ versus y_1 curves for different structural parameters. $y_2 = 0$ is prescribed in computations due to the fact that (i) the vibration of the satellite platform, i.e. y_2 , is orders of magnitude smaller than that of the capture mechanism, i.e. y_1 ; and (ii) y_1 and y_2 appear together in $D(y_1, y_2)$ and have a simple subtraction relation so that varying the value of $y_1 - y_2$ in Eq. (23) can be realized by merely varying y_1 .

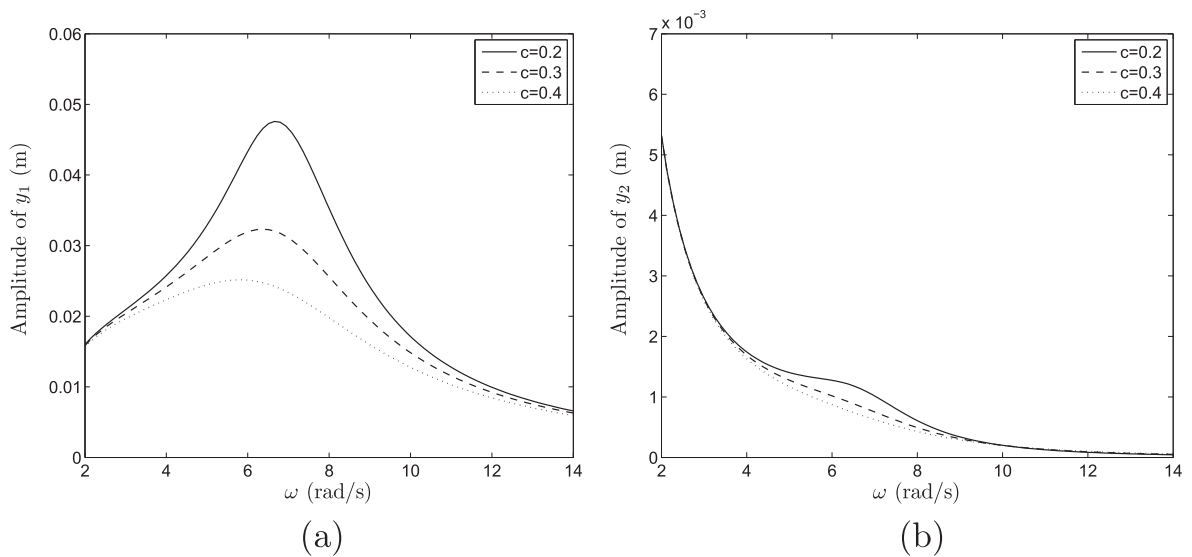


Fig. 13. Amplitudes of (a) y_1 and (b) y_2 versus ω for different friction coefficient c .

It is seen from Fig. 7 that a larger assembly angle θ_0 , smaller layer number n and rod length l increase the nonlinear damping, which is beneficial to isolation. It should be noted that increasing n does not increase the damping but decrease it instead. This can be intuitively explained that once more layers are included for a given quantity of relative motion between y_1 and y_2 , the rotation angle decreases which has an effect of reducing the damping. In sum, nonlinear damping can be flexibly designed via smartly choosing structural parameters, and the isolation performance employing the nonlinear damping will show advantage over the linear case in the following numerical examples.

4.3. Verification of accuracy of HB method

The accuracy of the first order HB (marked as HB1) method is verified by comparing with the RK4 method. It is seen from Fig. 8 that the HB1 results agree very well with that of the RK4, which indicates HB1 is sufficiently accurate for solving the present dynamical system.

Fig. 8(a) shows that the amplitude y_1 -frequency response curve has a peak at around $\omega = 6.68$, which is close to the linear natural frequency $\Omega = 7.14$. It can also be seen that once the forcing frequency ω approaches zero, the amplitude approaches infinity. This can be explained by the fact that as $\omega \rightarrow 0$ the external force becomes a constant force so that the whole floating system will be pushed away constantly, hence both A_{y_1}, A_{y_2} go to infinity. In addition, the amplitude y_1 -frequency response curve has a minima at about $\omega = 1$, which indicates that the vibration of the capture mechanism is smallest. Fig. 8(b) shows that the amplitude of y_2 decreases monotonically with the increases of the forcing frequency. It can be seen from the inset of Fig. 8(b) that the vibration of satellite platform m_2 is about one order of magnitude smaller than that of the capture mechanism in the real working conditions.

4.4. Amplitude-frequency response of the BIQS isolator

The effects of system parameters on the dynamical responses of the present BIQS system are exhaustively studied by means of amplitude-frequency response curves. Note that the ultra low frequency range is not plotted due to the fact that $\omega \rightarrow 0$ leads to a dramatically increasing amplitude as stated above. On the other hand, the response will become extremely weak when the excitation frequency is much larger than the resonant frequency, as indicated in Fig. 9. Therefore, the present attention is mainly focused on the low frequency range.

4.4.1. Effect of structural parameters

In Figs. 10–12, the amplitude-frequency curves of y_1 and y_2 are plotted for different structural parameters.

Fig. 10 shows the amplitude-frequency curves with different number of layers n . Specifically, the maximum A_{y_1} with $n = 2, 3$ and 4 take place at $\omega = 6.68, 4.40$ and 3.12 , respectively, which are essentially the resonant frequencies. The natural frequencies $\Omega_{n=2,3,4}$ calculated by Eq. (22) are $7.14, 4.76$ and 3.57 , respectively, which are in accordance with the resonant frequencies. The maximum A_{y_1} with $n = 2, 3$ and 4 are $0.047, 0.116$ and 0.225 , revealing that increasing n raises the maximum amplitudes significantly. This can be explained by the fact that a larger n is corresponding to a smaller damping as revealed in Fig. 7(a). For analysis, the whole frequency range can be divided into low, medium and high frequency regions

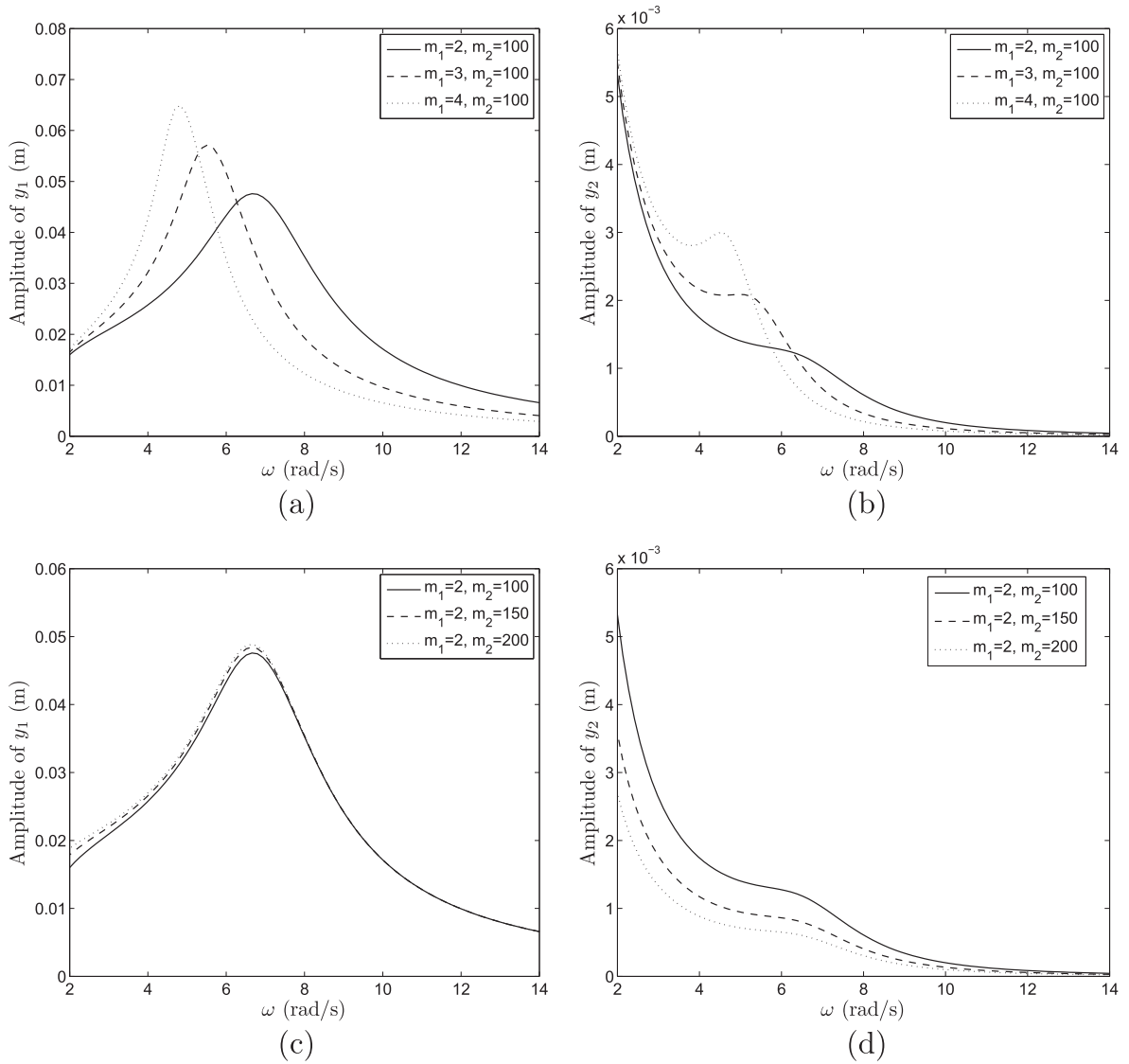


Fig. 14. Amplitudes of (a) y_1 and (b) y_2 versus ω for different values of m_1 ; amplitudes of (c) y_1 and (d) y_2 versus ω for different values of m_2 .

according to the relative magnitude of amplitudes. For A_{y_1} , the low frequency region is $\omega < 4.25$, in which $A_{y_1, n=2} < A_{y_1, n=3} < A_{y_1, n=4}$; and the high frequency region is $\omega > 6.68$ where $A_{y_1, n=2} > A_{y_1, n=3} > A_{y_1, n=4}$. Similar situations for A_{y_2} are observed in Fig. 10(b), where the low and high frequency regions are $\omega < 3.69$ and $\omega > 5.38$, respectively.

In practical space missions, the excitation frequencies are mainly distributed in from a few to a few hundreds hertz,¹ which can be regarded as high frequency excitation in the present system. Therefore, using more layers can improve the isolation performance of the BIQS. In addition, it can be seen from Fig. 10(a) and (b) that the magnitude of A_{y_2} is about two to three orders of magnitude smaller than that of A_{y_1} , which is very beneficial for on-orbit capture mission since the satellite platform that carrying many precision instruments needs to be very stable during the whole mission.

In Fig. 11, the effects of assembly angles θ_0 are investigated. Concretely, the resonant frequencies of y_1 for $\theta_0 = \pi/6$, $\pi/4$ and $\pi/3$ occur at $\omega = 6.68$, 11.93 and 20.67 in Fig. 11(a), respectively, which are consistent with the linear natural frequencies 7.14, 12.37 and 21.42 calculated by Eq. (22). Specifically, the relative errors between the resonant frequencies and the linear natural frequencies are 6.44%, 3.55% and 3.50%, which means using the natural frequencies calculated from the corresponding linear system is reasonable. Correspondingly, the maximum amplitudes are 4.7×10^{-2} , 1.8×10^{-2} and

¹ In particular, the moving payloads such as flywheels and gyros account for the frequency range from a few tens to hundreds hertz, the flexible structure such as antennas and solar arrays are from a few to a few tens hertz as reported in Ref. [10].

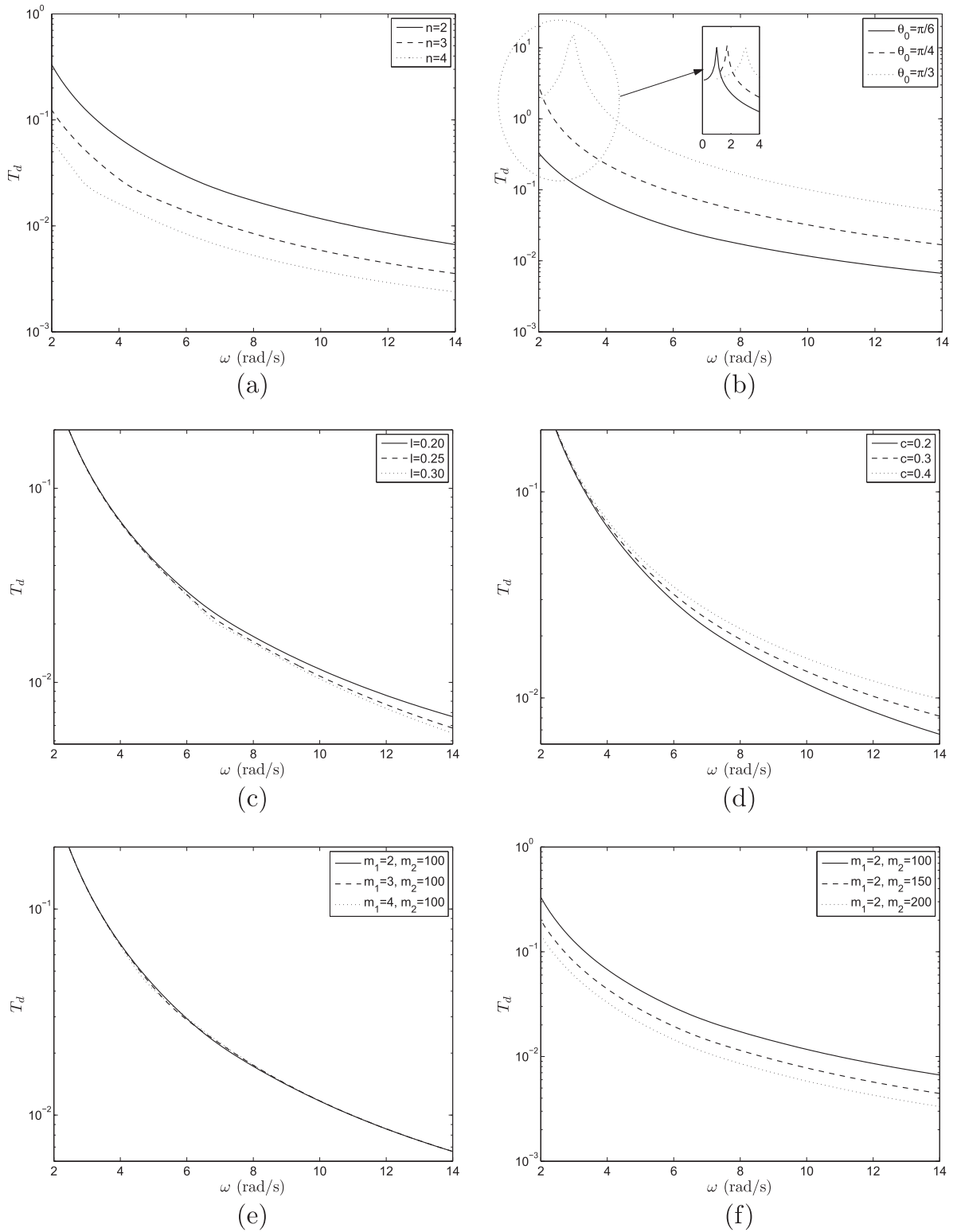


Fig. 15. Displacement transmissibility T_d versus ω for different (a) number of layers n ; (b) assembly angles θ_0 ; (c) rod length l ; (d) friction coefficient c ; (e) mass of satellite platform m_1 ; (f) mass of capture mechanism m_2 . Note that y-axis is plotted with logarithmic scale.

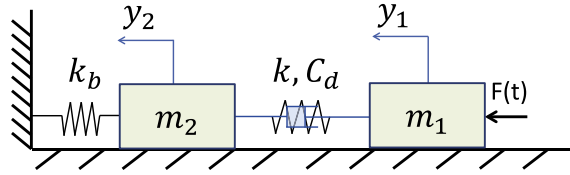


Fig. 16. Schematic diagram of the SMD isolator. Air drag and ground friction are zero, and the left spring is used during the modeling, and removed later to simulate the in space floating environment, i.e. $k_b = 0$.

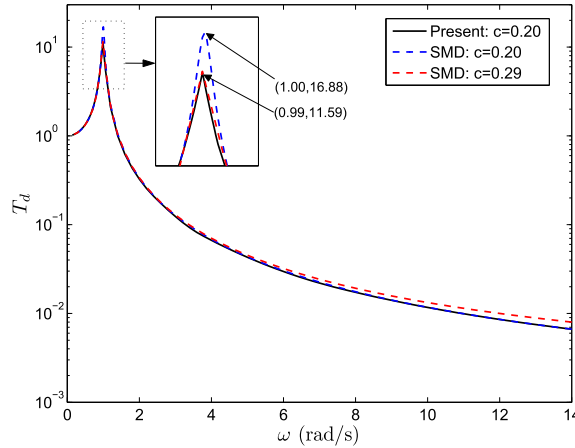


Fig. 17. Comparison of the displacement transmissibility versus forcing frequency curves between the present BIQS and the SMD isolators.

5.2×10^{-3} , indicating that increasing the assembly angle decreases the maximum amplitudes significantly. This can be explained by Fig. 7(b) that the system damping becomes larger as the assembly angle increases. For A_{y_1} , the low frequency region is $\omega < 11.93$, in which $A_{y_1, \theta_0=\frac{\pi}{6}} > A_{y_1, \theta_0=\frac{\pi}{4}} > A_{y_1, \theta_0=\frac{\pi}{3}}$; and the high frequency region is $\omega > 20.67$, in which $A_{y_1, \theta_0=\frac{\pi}{6}} < A_{y_1, \theta_0=\frac{\pi}{4}} < A_{y_1, \theta_0=\frac{\pi}{3}}$; the medium region $\omega \in (11.93, 20.67)$ is a transition region. The frequency responses of y_2 are given in Fig. 11(b). It can be seen by comparing with Fig. 11(a) that the magnitude of A_{y_2} is about two to three orders of magnitude smaller. Since the vibration source in space is mostly high frequency, hence it is preferable to choose a relatively small assembly angle θ_0 in practical applications to better suppress vibrations.

Shown in Fig. 12 are the frequency response curves with different values of rod length l . It indicates that the rod length has a significant influence on the amplitude-frequency responses around the resonant frequency. In specific, a smaller rod length l is corresponding to a weaker vibration in the neighborhood of $\omega = 6.68$, which is consistent with Fig. 7(c) that the system damping becomes larger with a smaller l . So, it is concluded that a smaller isolator with shorter rod not only enjoys a lower weight, but also has a better isolation performance. On the other hand, the resonant frequencies for different values of l are the same, which verifies the previous finding that the natural frequency is independent of l . In practical applications, the size of the rods can also be adjusted according to the requirement of the problem under current consideration. However, the weight of the rods should be relatively small compared with the objects m_1 and m_2 . As for the potential applications of the BIQS system for micro-/nano-scale structures, the connecting rods of the BIQS system should be designed and manufactured in much lighter materials, such as aluminium alloy or carbon fiber etc., to alleviate potential influence in dynamic responses.

In summary, it can be concluded that a larger layer number n , a smaller assembly angle θ_0 and a smaller rod length l can suppress the vibrations of both satellite platform and capture mechanism.

4.4.2. Effect of friction coefficient

The influences of damping c on the frequency responses are compared in Fig. 13. It can be seen that increasing the system damping reduces the response amplitudes, especially around the resonant frequency. In particular, the resonant frequencies for $c = 0.2, 0.3$ and 0.4 are $\omega = 6.66, 6.37$ and 5.81 respectively, see Fig. 13(a). However, the natural frequency calculated by Eq. (22) does not depend on damping c . Thus, the difference between the natural frequency and the resonant frequency demonstrates that the damping of a system can slightly influence its natural frequency, it is for convenience that the natural frequency is calculated directly by $|\mathbf{K} - \Omega^2 \mathbf{M}| = 0$ without considering damping. The maximum amplitudes $A_{y_1, c=0.2}, A_{y_1, c=0.3}$ and $A_{y_1, c=0.4}$ are $0.048, 0.032$ and 0.025 , which is approximately inversely proportional to damping.

Fig. 13(a) shows that the damping c only has an influence on A_{y_2} in a limited frequency region about $\omega \in (3.8, 9.5)$, beyond which the damping does not notably take effect.

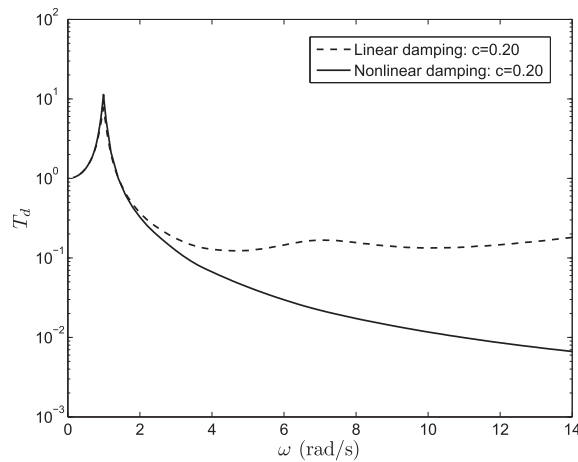


Fig. 18. Comparison of the displacement transmissibility versus forcing frequency curves of the present BIQS isolator with nonlinear and linear dampings.

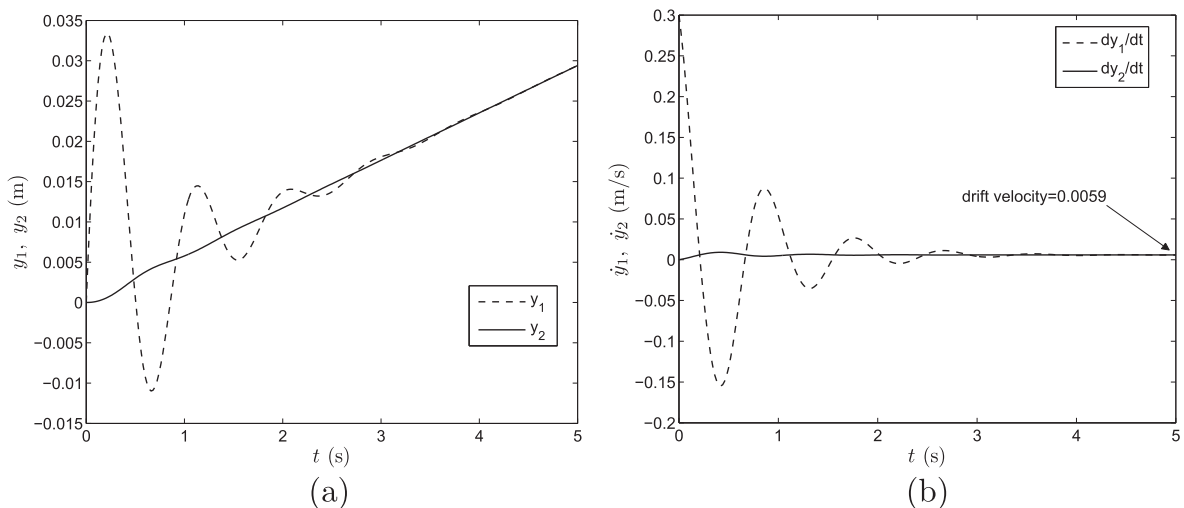


Fig. 19. (a) Time histories of y_1 and y_2 ; and (b) velocity histories of y_1 and y_2 subject to an impulse $I = 0.6$.

4.4.3. Effect of masses

The effects of m_1 on the response are revealed in Fig. 14(a) and (b), and that of m_2 are in Fig. 14(c) and (d).

It is seen from Fig. 14(a) that the resonant frequencies for $m_1 = 2, 3$ and 4 are obviously different. On the contrary, the resonant frequencies for different m_2 's are almost the same. Since $\Omega \stackrel{\text{def}}{=} \sqrt{k_{eq}/m_{eq}}$, comparing to Eq. (22) yields $k_{eq} = \alpha_1$ and $m_{eq} = m_1 m_2 / (m_1 + m_2)$. In this study, $m_1 \ll m_2$, so $m_1 + m_2 \approx m_2$ thus $m_{eq} \approx m_1$. Therefore, the resonant frequency is mostly dependent on m_1 and the influence of m_2 is negligible, which is verified by Fig. 14(a) and (c). Specifically, the resonant frequencies for $m_1 = 2, 3$ and 4 are 6.68, 5.53 and 4.82, and the corresponding amplitudes are 0.048, 0.057 and 0.065, respectively. Both Fig. 14(a) and (b) show that a larger m_1 is corresponding to a smaller vibration amplitude in the high frequency region. Therefore, it is concluded that increasing m_1 can reduce the resonant frequency as well as suppress vibrations in high frequency region.

Interestingly, it is seen from Fig. 14(c) that the value of m_2 has little impact on the response of y_1 , which reflects that varying the mass of the satellite platform does not affect the vibration of the capture mechanism significantly. However, the vibration of the capture mechanism y_2 is significantly reduced with the increase of mass of the satellite platform m_2 , as shown in Fig. 14(d).

In sum, it is preferable to use heavier satellite platform and capture mechanism with regard to vibration suppressions. However, a heavier spacecraft inevitably leads to more launching cost.

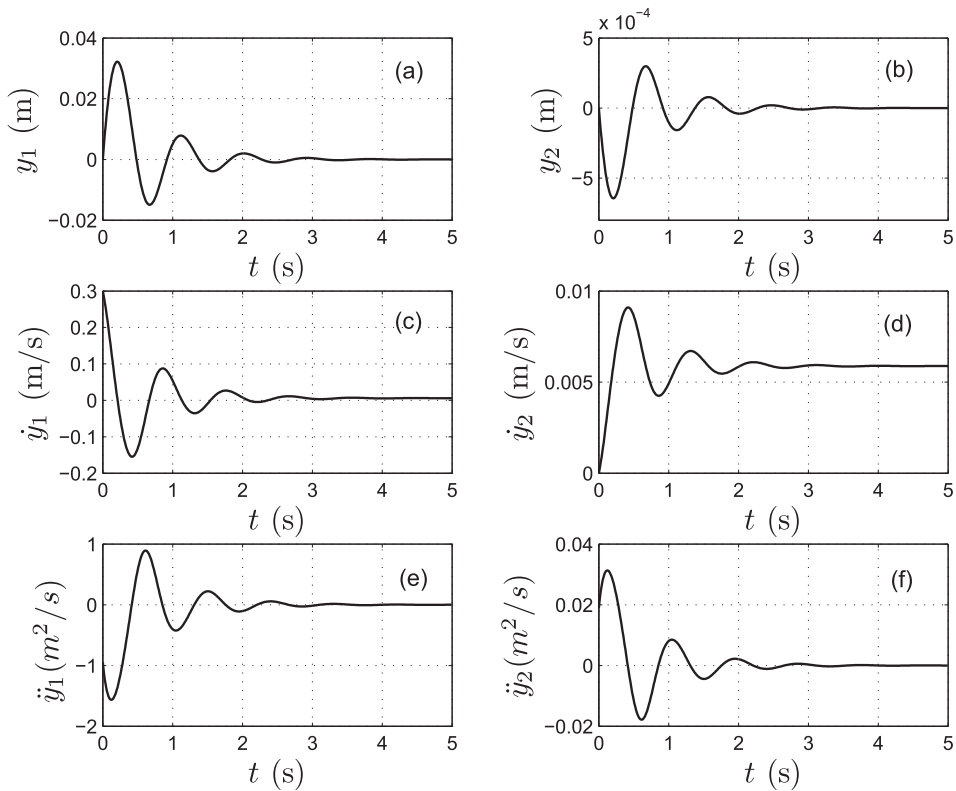


Fig. 20. (a) Time history of y_1 ; (b) time history of y_2 ; (c) velocity of \dot{y}_1 ; (d) velocity of \dot{y}_2 ; (e) acceleration of \ddot{y}_1 ; (f) acceleration of \ddot{y}_2 subject to an impulse $I = 0.6$. Note that the drifting motions have been eliminated in (a) and (b); (b) and (d) re-plotted from Fig. 19 separately to avoid being drowned out by (a) and (c).

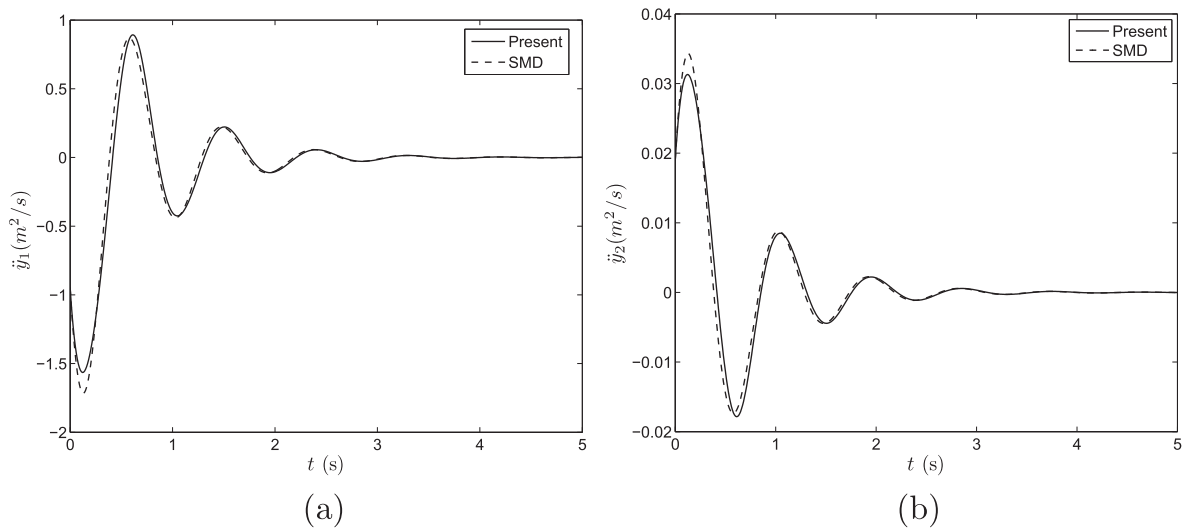


Fig. 21. Comparisons of the (a) acceleration \ddot{y}_1 ; and (b) acceleration \ddot{y}_2 for the present BIQS and the SMD isolators.

4.4.4. Displacement transmissibility

The displacement transmissibility is denoted by T_d herein and defined as the ratio between the vibration amplitude of y_2 and that of y_1 , i.e. $T_d = A_{y_2}/A_{y_1}$.

Shown in Fig. 15(a)–(f) are T_d versus ω curves for different parameters. In each subfigure, the system parameters are chosen as the reference values given above except the one under current consideration. It can be seen from Fig. 15(a), (b) and (f)

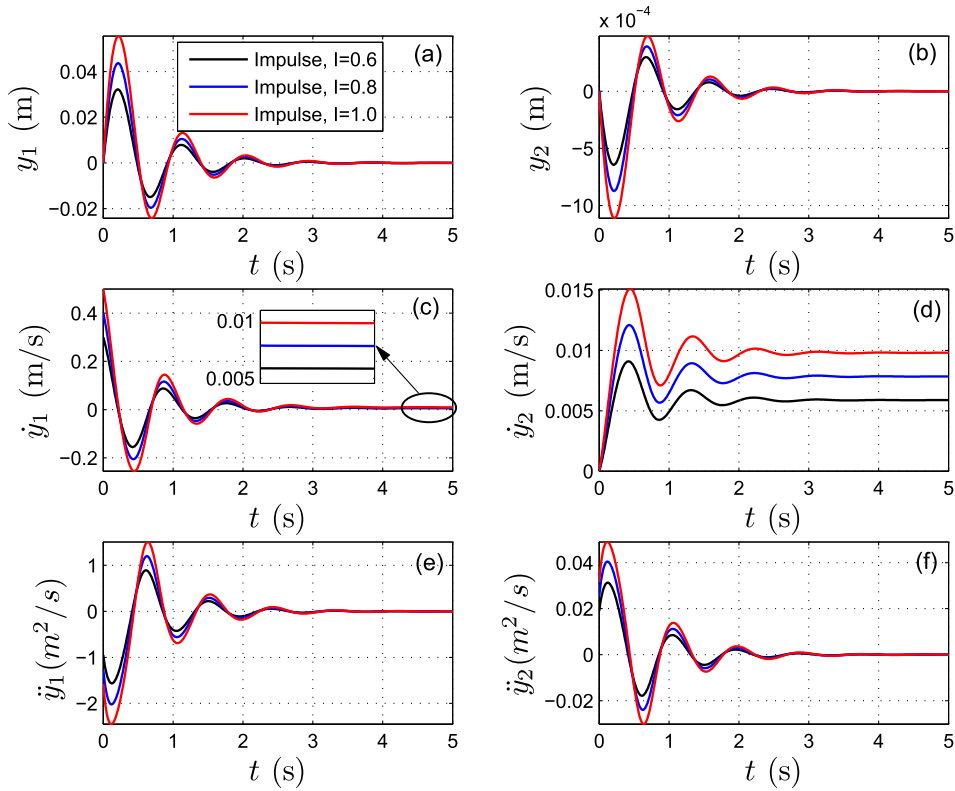


Fig. 22. Comparisons of (a) displacement y_1 ; (b) displacement y_2 ; (c) velocity \dot{y}_1 ; (d) velocity \dot{y}_2 ; (e) acceleration \ddot{y}_1 ; (f) acceleration \ddot{y}_2 evolving with time t for the present BIQS system subject to impulses of different magnitudes.

that a larger n , a smaller θ_0 , a larger m_2 are corresponding to lower displacement transmissibility T_d , which is beneficial to isolation. It can be seen from Fig. 15(c) and (d) that varying rod length l and damping c does not affect the displacement transmissibility in the low frequency region, e.g. $\omega < 5$ for $l, \omega < 3.5$ for c . Nevertheless, in the higher frequency region, increasing l and decreasing c can lower the displacement transmissibility. Fig. 15(e) shows that the mass of the capture mechanism m_1 does not influence the displacement transmissibility significantly.

It should be emphasized that the displacement transmissibility measures the relative magnitude between the vibrations of the platform and the capture mechanism.

4.5. Comparison with SMD isolator

In this section, the presently proposed BIQS isolator is compared with the typical SMD system as shown in Fig. 16. The dynamical system are established by Lagrange's equations. The kinetic energy, potential energy and the virtual work done by nonconservative forces are

$$T = \frac{1}{2} m_1 \dot{y}_1^2 + \frac{1}{2} m_2 \dot{y}_2^2,$$

$$V = \frac{1}{2} k_b y_2^2 + \frac{1}{2} k (y_1 - y_2)^2,$$

$$\delta W = C_d (\dot{y}_2 - \dot{y}_1) \delta y_1 - C_d (\dot{y}_2 - \dot{y}_1) \delta y_2 + F \delta y_1.$$

Substituting the above quantities into the Lagrange's equations, the dynamical system of the SMD isolator is

$$m_1 \ddot{y}_1 + C_d (\dot{y}_1 - \dot{y}_2) + k (y_1 - y_2) = F(t), \quad (25)$$

$$m_2 \ddot{y}_2 - C_d (\dot{y}_1 - \dot{y}_2) - k y_1 + (k + k_b) y_2 = 0. \quad (26)$$

In order to conduct a fair comparison between the BIQS isolator and the typical SMD isolator, system parameters of the SMD system should be reasonably selected. Herein, m_1 , m_2 , k_b and $F(t)$ are the same as that in the BIQS system, while the damping coefficient C_d and stiffness k are chosen to be the linearized damping γ_0 and linearized stiffness α_1 in Eqs. (19) and (20), respectively.

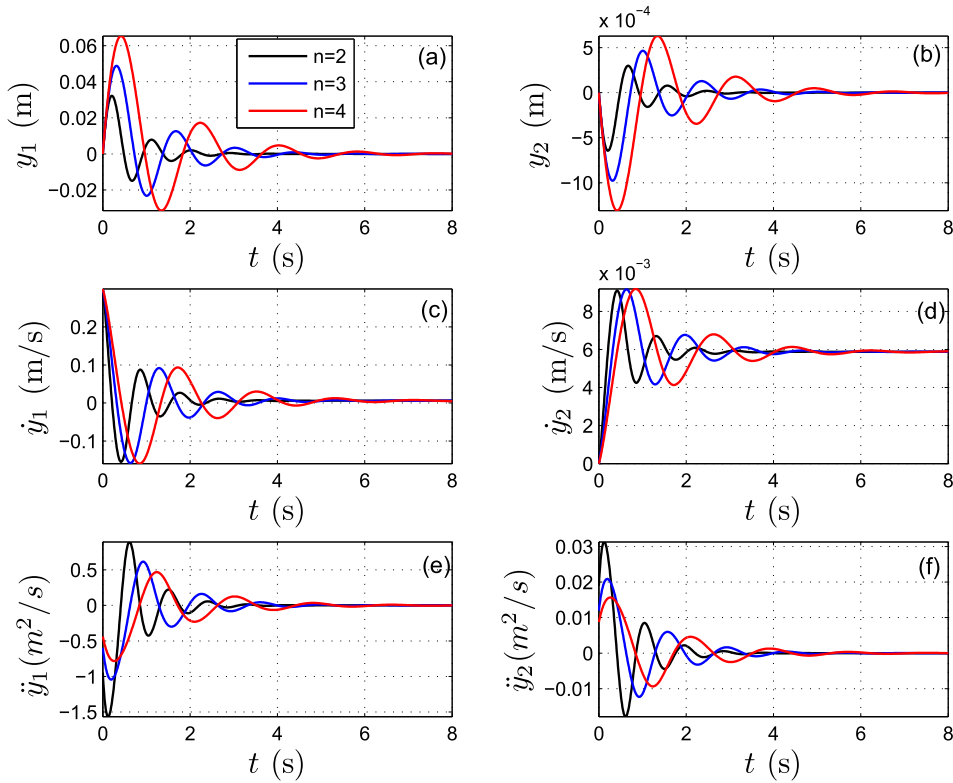


Fig. 23. Comparisons of (a) displacement y_1 ; (b) displacement y_2 ; (c) velocity \dot{y}_1 ; (d) velocity \dot{y}_2 ; (e) acceleration \ddot{y}_1 ; (f) acceleration \ddot{y}_2 evolving with time t for the present BIQS system with different values of n .

Fig. 17 shows the displacement transmissibility versus forcing frequency curves for the present and the SMD isolators. It is seen that the SMD result is in agreement with that of the present isolator except in the frequency region around $\omega = 1$ where a peak takes place. Enlargement in the inset plot shows that the maximum T_d of the present and the SMD isolators with $c = 0.2$ are 11.59 and 16.88, respectively, verifying a better performance of the present BIQS isolator. When the damping c is enhanced to 0.29 the maximum value of the SDM is suppressed to the same level of the BIQS with $c = 0.2$. Under this circumstance, however, T_d of the SMD becomes higher than that of the BIQS in the high frequency region.

Therefore, it is concluded that the presently proposed BIQS isolator has a better isolation performance than the classical SMD isolator in the high frequency region.

In the above, the combined effects of nonlinear damping and stiffness on the isolation performance are investigated. Next, the effect of sole nonlinear damping will be studied by merely neglecting the nonlinear damping component $\gamma_1(y_1 - y_2) + \gamma_2(y_1 - y_2)^2 + \gamma_3(y_1 - y_2)^3$ in the governing Eqs. (19) and (20). It can be seen from Fig. 18 that the curves of the two models agree well in the low frequency region, i.e. $\omega < 2$. In the high frequency region, however, the BIQS system with nonlinear damping shows a much better performance than its linear damping counterpart.

4.6. BIQS system subject to impulsive force

In on-orbit servicing missions, successfully capturing the target is a critical step. The relative velocity between the chaser and the target is always greater than zero, thus collision is inevitable. To simulate the post-capture responses, the BIQS system subject to an impulsive force $\hat{F}(t)$ is analyzed in this section. According to Section 2.3, the effect of $\hat{F}(t)$ can be replaced by imposing an impulse I to the capture mechanism.² Since the dynamical response in this situation is no longer periodic, the RK4 method is employed instead. In computations, the system parameters are $m_1 = 2$, $m_2 = 100$, $k = 1200$, $n = 2$, $\theta_0 = \pi/6$, $l = 0.2$, $c = 0.2$, $C_d = 0.1$ and $I = 0.6$, unless otherwise mentioned. The SI units are omitted for brevity.

Fig. 19 provides the time histories and velocity histories subject to an impulse. It can be seen that both curves of y_1 and y_2 vibrate around an oblique line, which implies that the motions consist of simultaneous vibrational and translational components. In addition, the two time history curves approach to the oblique line eventually, indicating that the vibrational component has been damped out with time. The curves of \dot{y}_1 and \dot{y}_2 evolving with time are plotted in Fig. 19(b). It is seen that the

² Note that the mass of the capture mechanism m_1 actually includes the mass of the target.

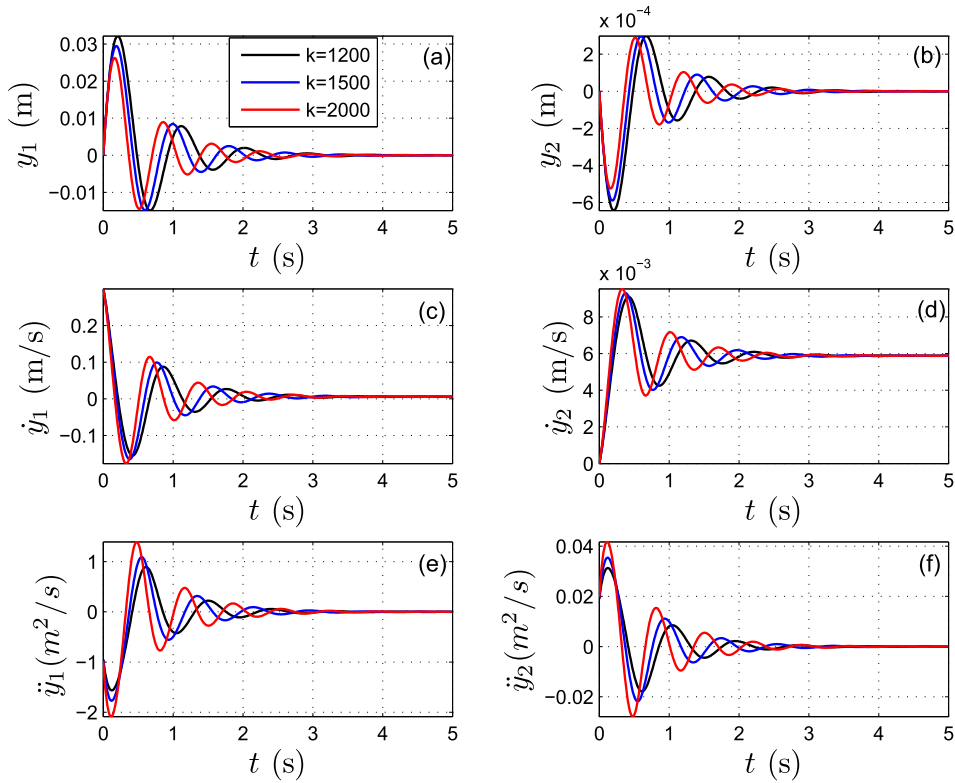


Fig. 24. Comparisons of (a) displacement y_1 ; (b) displacement y_2 ; (c) velocity \dot{y}_1 ; (d) velocity \dot{y}_2 ; (e) acceleration \ddot{y}_1 ; (f) acceleration \ddot{y}_2 evolving with time t for the present BIQS system with different values of k .

initial velocity of \dot{y}_1 is 0.3, which is caused by the impulse I acted on m_1 . The $|\dot{y}_2|_{\max}$ is very small in comparison with $|\dot{y}_1|_{\max}$. It should be noted that the two masses do not stay put, but drift at a speed of $v_d = 5.91$ cm/s eventually.

To better understand the motions in each freedom, the time histories, velocities and accelerations of \dot{y}_1, \dot{y}_2 are plotted in Fig. 20. In the plotting, the drifting motions, representing the translations in space, have been eliminated to highlight the vibrational motions. It is seen that the vibrations of the two masses have been completely damped out in about four seconds. Specifically, the $|y_1|_{\max}$ and $|y_2|_{\max}$ are 3.2×10^{-2} and 6.4×10^{-4} , respectively, which is satisfactory. Fig. 20(c) and (d) show that the maximum velocities $|\dot{y}_1|_{\max}, |\dot{y}_2|_{\max}$ are 0.3 and 9.1×10^{-3} , respectively. $|\dot{y}_1|_{\max}$ takes place at the $t = 0$ at the time it suffers an impulse, while \dot{y}_2 starts from still and goes to the maximum value in 0.5 s. $|\dot{y}_2|_{\max}$ is smaller than 1 cm/s which is well performed.

The most important indicator for evaluating vibrations is the acceleration, because the inertial force acting on the instruments mounted on satellite is proportional to acceleration. It can be seen from Fig. 20(e) and (f) that $|\ddot{y}_1|_{\max}$ and $|\ddot{y}_2|_{\max}$ are 1.5 and 0.03, respectively. So, the acceleration of the satellite platform is less than 3.1 mg which is very satisfactory.

4.6.1. Comparison with the SMD isolator

The isolation performances of the BIQS and the traditional SMD isolators are compared in Fig. 21, which shows that the maximum accelerations of \ddot{y}_1 for the BIQS and the SMD are 1.56 and 1.72, and that of \ddot{y}_2 are 0.0313 and 0.0343, respectively. In particular, the $|\ddot{y}_1|_{\max}$ and $|\ddot{y}_2|_{\max}$ of the SMD are 10.3% and 9.58% larger than that of the BIQS. It is concluded that the present BIQS isolator has a better performance than the traditional SMD.

4.6.2. Effect of impulse magnitude

The effect of the impulse level on dynamical responses is studied. In Fig. 22(a) and (b), the maximum amplitudes $|y_1|_{\max}$ are 0.32, 0.44, 0.56 and $|y_2|_{\max}$ are 6.42×10^{-4} , 8.73×10^{-4} , 11.11×10^{-4} for $I = 0.6, 0.8, 1.0$, respectively. This demonstrates that both the vibration amplitudes of y_1 and y_2 are proportional to the impulse magnitude. As for the velocities in Fig. 22(c) and (d), $|\dot{y}_1|_{\max}$ takes place at the starting time due to the impulse, and $|\dot{y}_2|$ for $I = 0.6, 0.8$ and 1.0 start from rest and go to the maxima 1.5×10^{-2} , 1.2×10^{-2} and 9.1×10^{-3} , respectively. The final drifting speeds of the \dot{y}_1 and \dot{y}_2 are exactly the same for each case, implying that the satellite platform and the capture mechanism finally translate at the same

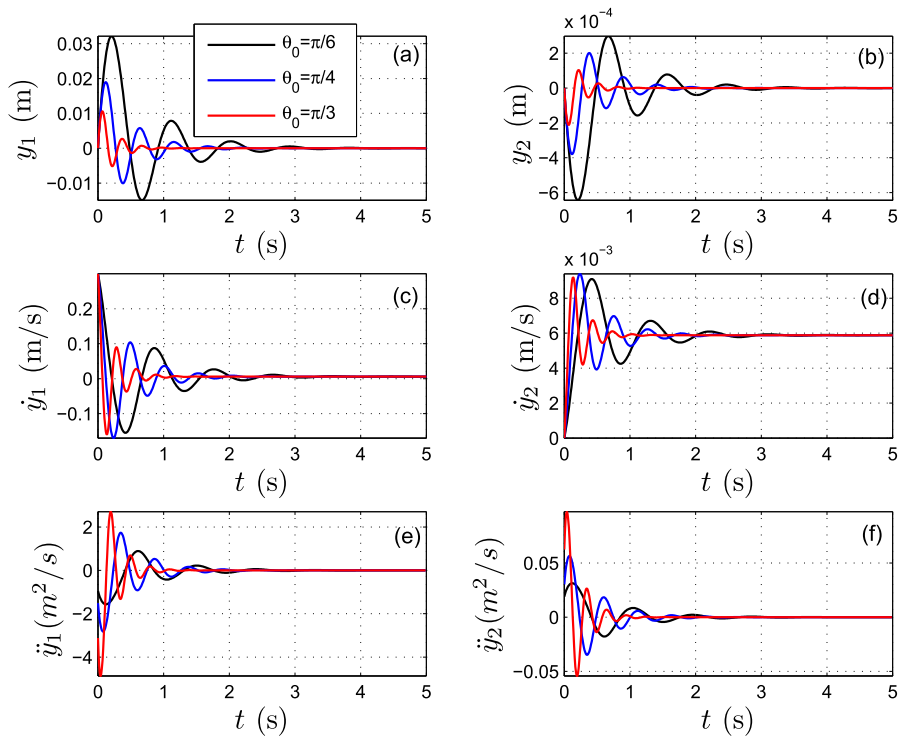


Fig. 25. Comparisons of (a) displacement y_1 ; (b) displacement y_2 ; (c) velocity \dot{y}_1 ; (d) velocity \dot{y}_2 ; (e) acceleration \ddot{y}_1 ; (f) acceleration \ddot{y}_2 evolving with time t for the present BQS system with different values of assembly angle θ_0 .

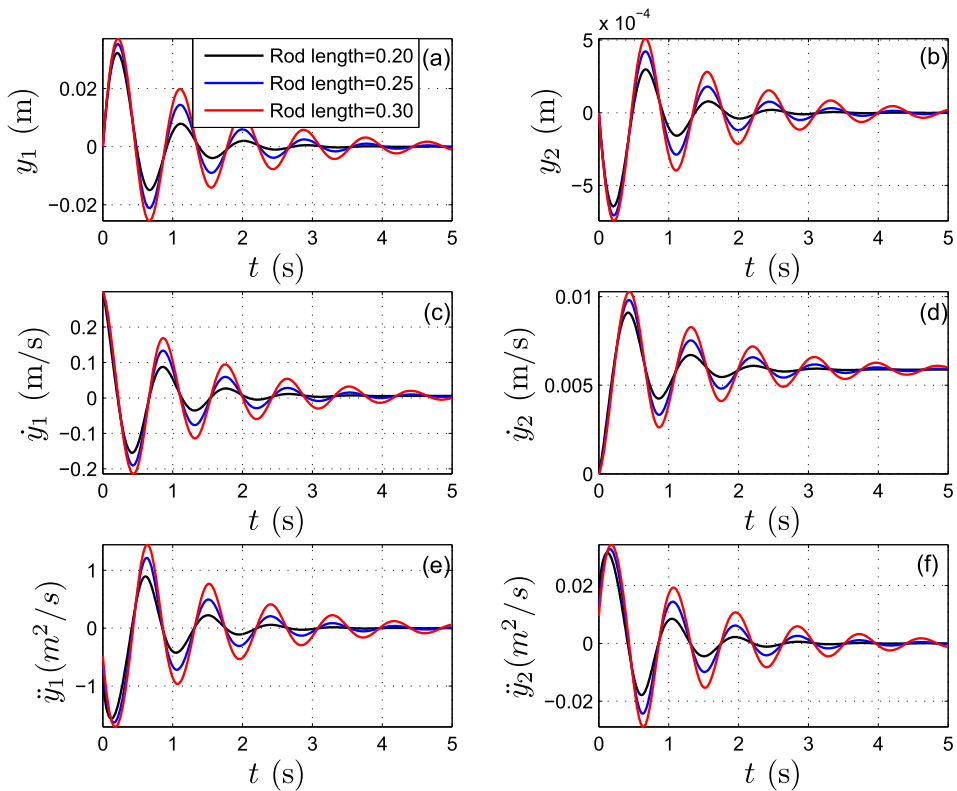


Fig. 26. Comparisons of (a) displacement y_1 ; (b) displacement y_2 ; (c) velocity \dot{y}_1 ; (d) velocity \dot{y}_2 ; (e) acceleration \ddot{y}_1 ; (f) acceleration \ddot{y}_2 evolving with time t for the present BQS system with different values of rod length l .

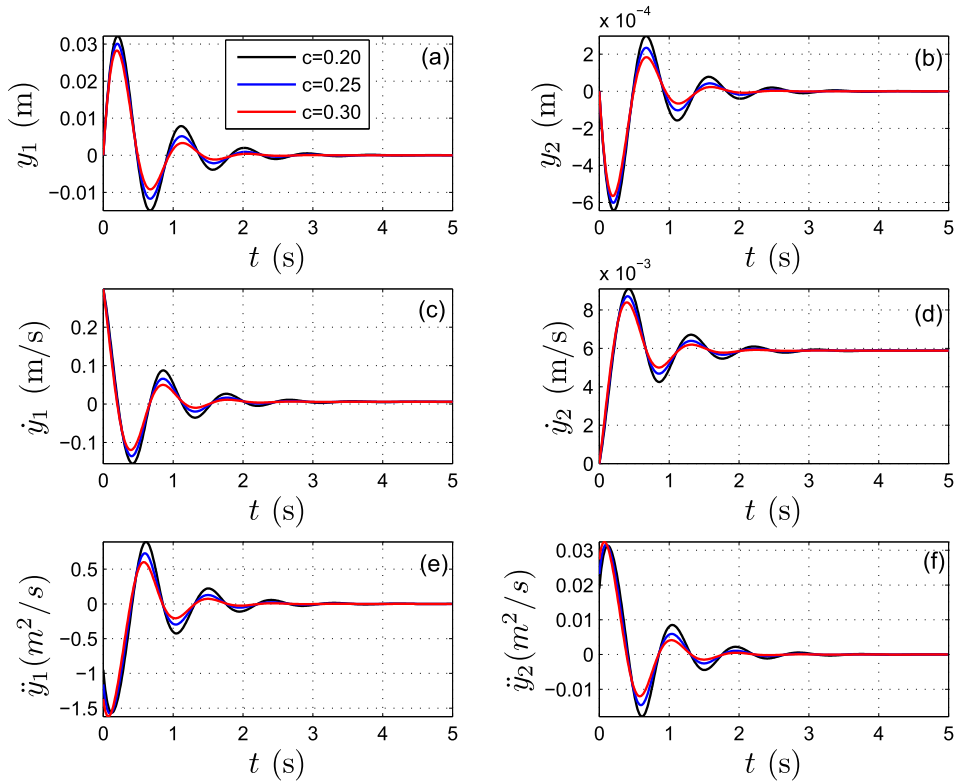


Fig. 27. Comparisons of (a) displacement y_1 ; (b) displacement y_2 ; (c) velocity \dot{y}_1 ; (d) velocity \dot{y}_2 ; (e) acceleration \ddot{y}_1 ; (f) acceleration \ddot{y}_2 evolving with time t for the present BIQS system with different values of friction coefficient c .

speed. Fig. 22(e) and (f) show the curves of accelerations evolving with time, in which $|\ddot{y}_1|_{\max}$ are 0.90, 1.21, 1.51 and $|\ddot{y}_2|_{\max}$ are 0.031, 0.040, 0.049 for $I = 0.6, 0.8, 1.0$.

It is concluded that the magnitudes of displacement, velocity and acceleration are proportional to the impulse level, while the decay time only slightly increases with the increase of impulse magnitude.

4.6.3. Effect of structural parameters

The effects of structural parameters, namely layer number n , stiffness k , assembly angle θ_0 , rod length l , on the dynamical responses of the BIQS system are thoroughly studied in this section.

Shown in Fig. 23 are the response curves for different values of layer number n . It can be seen from Fig. 23(a) and (b) that increasing n raises the amplitudes of both the platform and the capture mechanism, as well as increases the decay time. However, the magnitudes of the velocities \dot{y}_1 and \dot{y}_2 are not significantly influenced as shown in Fig. 23(c) and (d). More importantly, the accelerations are investigated in Fig. 23(e) and (f), which show that the maximum accelerations for $|\ddot{y}_1|$, $n = 2, 3, 4$ are 1.56, 1.04, 0.78, and that for $|\ddot{y}_2|$, $n = 2, 3, 4$ are 0.0313, 0.021, 0.0156 respectively. It shows that a larger n leads to a smaller acceleration for both m_1 and m_2 . Therefore, it is concluded that increasing the number of layers can suppress the accelerations of the satellite platform and the capture mechanism, but on the other hand extends the decay time.

The influences of the stiffness k are investigated in Fig. 24. It can be seen from Fig. 24(a) and (b) that increasing k can slightly decrease the amplitude of y_1 while the amplitude of y_2 remains at the same level. Fig. 24(c) and (d) show that the velocity magnitudes are almost the same for both objects, and the stiffness does not alter the final drifting speed. It is emphasized that a larger k results in a larger acceleration, see Fig. 24(e) and (f). In specific, the accelerations of m_1 for $k = 1200, 1500, 2000$ are 1.56, 1.77, 2.09, and are 0.0313, 0.035, 0.0416 for m_2 . Moreover, the decay time does not change with the stiffness k . So, it is found that decreasing the stiffness k is beneficial to the isolation performance of the BIQS system.

Fig. 25 provides a series of response curves for different assembly angles. It can be seen from Fig. 25(a) and (b) that increasing θ_0 results in smaller vibration amplitudes, as well as shortens the decay time. The maximum velocities are not notably influenced by θ_0 as shown in Fig. 25(c) and (d). On the other hand, increasing θ_0 leads to a larger acceleration for both the platform and the capture mechanism, which is undesired. In this case, the maximum acceleration of the platform with $\theta_0 = \pi/3$ is about three times larger than that with $\theta_0 = \pi/6$, which means the isolation performance is very sensitive to

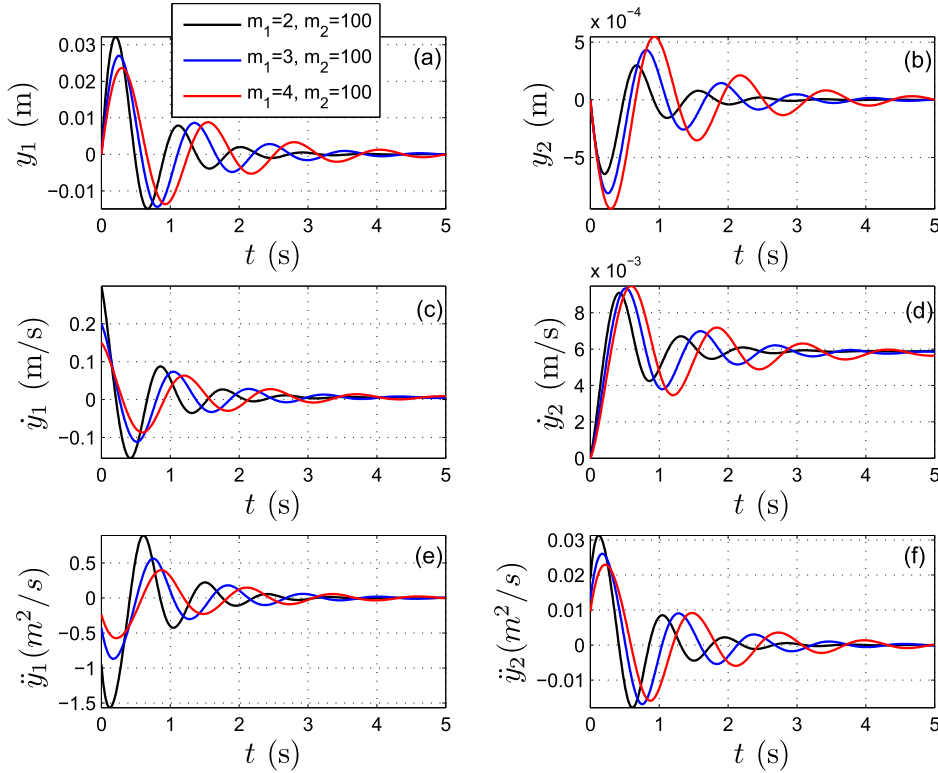


Fig. 28. Comparisons of (a) displacement y_1 ; (b) displacement y_2 ; (c) velocity \dot{y}_1 ; (d) velocity \dot{y}_2 ; (e) acceleration \ddot{y}_1 ; (f) acceleration \ddot{y}_2 evolving with time t for the present BIQS system with different values of m_1 .

the assembly angle. Therefore, it is recommended to choose a smaller assembly angle to suppress accelerations, but at the expense of a longer decay time.

The effects of the rod length l are explored in Fig. 26. It can be seen that decreasing the rod length can (i) reduce the amplitudes, the maximum velocities, and the maximum accelerations of both m_1 and m_2 ; (ii) shorten the decay time. Thus, a shorter rod is preferable in the design of BIQS system provided that the material strength and the working stroke are satisfied.

4.6.4. Effect of friction coefficient

In Fig. 27, the effects of the friction coefficient c on the responses are investigated. It shows that increasing c can lower the vibration amplitudes, velocities, and accelerations. Besides, the decay time can also be reduced with a larger c .

Hence, increasing the friction coefficient of the joints is beneficial to the isolation performance.

4.6.5. Effect of masses

The masses of the satellite platform and the capture mechanism are important elements in the BIQS system. In this section, the effects of m_1 and m_2 on the isolation performance are studied. In Fig. 28, m_1 is varied while m_2 keeps constant, and vice versa in Fig. 29.

Fig. 28 shows that increasing m_1 can decrease the vibration amplitude and the maximum velocity of m_1 , but on the contrary increase the vibration amplitude and maximum velocity of m_2 . Fortunately, the maximum accelerations of both m_1 and m_2 can be reduced with the increase of m_1 . Therefore, a better isolation performance can be achieved by using a heavier capture mechanism with a slightly longer decay time.

The influences of m_2 are revealed in Fig. 29. Interestingly, the variation of m_2 has little effect on the responses of m_1 in terms of either y_1 , \dot{y}_1 or \ddot{y}_1 . On the other hand, the isolation of m_2 itself benefits from a larger m_2 . As is seen from Fig. 29, increasing m_2 can reduce the vibration amplitude, the maximum velocity and acceleration of the satellite platform m_2 . In the meanwhile, the decay time can also be moderately shortened. Thus, it is concluded that the larger satellite platform is, the better the isolation performance would be. In practical projects, however, the mass of the satellite is strictly restricted due to the expensive launching cost per unit mass.

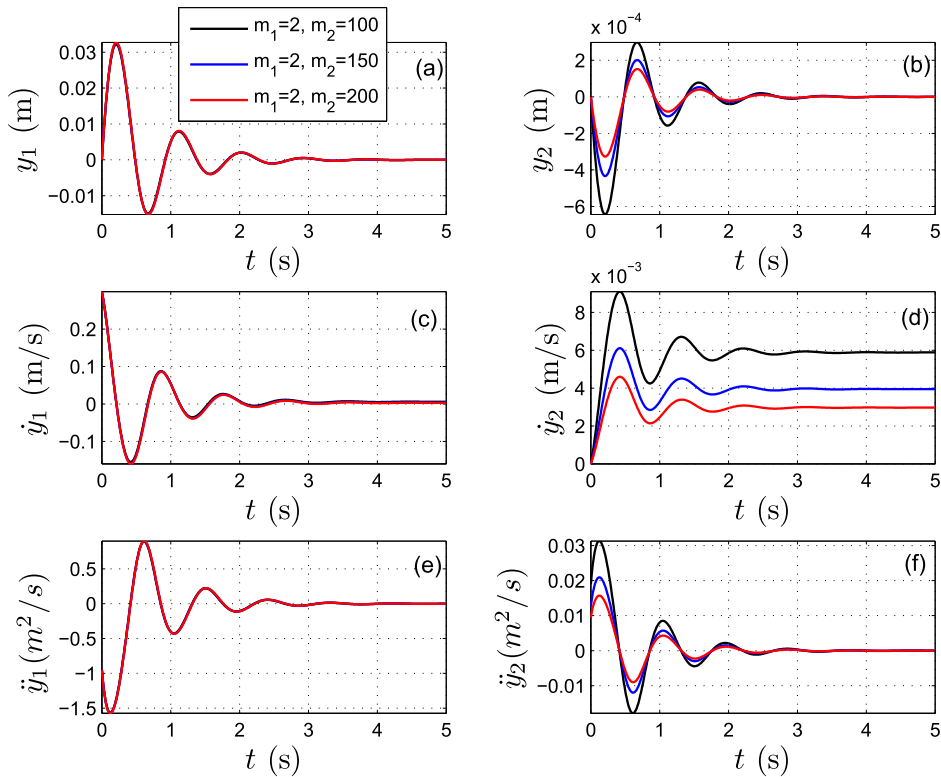


Fig. 29. Comparisons of (a) displacement y_1 ; (b) displacement y_2 ; (c) velocity \dot{y}_1 ; (d) velocity \dot{y}_2 ; (e) acceleration \ddot{y}_1 ; (f) acceleration \ddot{y}_2 evolving with time t for the present BIQS system with different values of m_2 .

5. Conclusions

The bio-inspired quadrilateral shape (BIQS) isolation system is proposed to suppress the micro-vibrations of a free-floating spacecraft subject to either periodic or impulsive forces. The governing equations of the present system, which is essentially a two DOF under-constrained nonlinear dynamical system, are established via Lagrange's equations. Efficient performance of the BIQS isolator has been verified through comparisons with the conventional spring-mass-damper (SMD) isolator. In addition, the beneficial effect of nonlinear damping has been demonstrated by comparing with its counterpart retaining only linear damping. In numerical simulations, the frequency-response, displacement transmissibility and time-response curves were employed for comparison purpose. The influences of various system parameters on the isolation performance for both the satellite platform and the capture mechanism have been thoroughly investigated for the BIQS system under either periodic or impulsive excitations. Several conclusions can be drawn from numerical simulations.

- Using a larger layer number n , a smaller assembly angle θ_0 or stiffness k decreases the vibration magnitudes of both the platform and capture mechanism under either a high-frequency periodic or an impulsive force, but at the expense of a longer decay time. Among these, θ_0 is the most sensitive parameter, and then are n and k in sequence.
- Decreasing the rod length l can reduce the amplitudes, the maximum velocities, and the maximum accelerations of both objects, as well as shorten the decay time. Thus, a shorter rod is preferable in the design of the BIQS isolator under the premise that the material strength and the working stroke are satisfied.
- Using heavier satellite platform and capture mechanism is beneficial to isolation performance. Specifically, (i) increasing the mass of the platform can better suppress the system vibrations under high frequency excitations, while increasing the mass of capture mechanism can suppress the platform vibration in the whole frequency range, but does not notably affect the capture mechanism; (ii) increasing m_1 and m_2 can decrease the maximum accelerations of both objects in case of impulsive forces.
- The BIQS isolator is superior to the classical SMD isolator by about 10% in terms of acceleration amplitudes. Specifically, the maximum accelerations of various BIQS systems (set $\theta_0 = \pi/6$) is 40.8 mg, which is very satisfactory. Besides, the isolation performance of BIQS with nonlinear damping shows a much better performance than its counterpart with linear damping.

Overall, the isolation performance of the presently proposed BIQS isolation system can be flexibly adjusted via smartly choosing different values of system parameters. The BIQS system offers a highly efficient passive control approach for post-capture vibration isolations of spacecraft. However, the present system is limited to the simulation of on-orbit capture in the axial direction, future studies may be focused on the three dimensional capture and experimental analyses of the BIQS system.

Acknowledgements

This study is financially supported by Chinese NSF (Nos. 11502203, 11402200), and the General Research Fund of Hong Kong RGC (15206717). The first author wishes to thank the supports from Hong Kong Scholar and NPU Aoxiang New Star Projects.

References

- [1] J.H. Saleh, E.S. Lamassoure, D.E. Hastings, D.J. Newman, Flexibility and the value of on-orbit servicing: new customer-centric perspective, *J. Spacecraft Rockets* 40 (2) (2003) 279–291.
- [2] A. Badawy, C.R. McInnes, On-orbit assembly using superquadric potential fields, *J. Guid. Control Dyn.* 31 (1) (2008) 30.
- [3] R.B. Friend, Orbital express program summary and mission overview, *Sensors and Systems for Space Applications II*, vol. 6958, International Society for Optics and Photonics, 2008, p. 695803.
- [4] E. Stoll, J. Letschnick, U. Walter, J. Artigas, P. Kremer, C. Preusche, G. Hirzinger, On-orbit servicing, *IEEE Robotics Autom. Mag.* 16 (4) (2009).
- [5] S.I. Nishida, S. Kawamoto, Y. Okawa, F. Terui, S. Kitamura, Space debris removal system using a small satellite, *Acta Astronaut.* 65 (1) (2009) 95–102.
- [6] C. Bombardelli, J. Pelaez, Ion beam shepherd for contactless space debris removal, *J. Guid. Control Dyn.* 34 (3) (2011) 916.
- [7] M.M. Castronuovo, Active space debris removal – a preliminary mission analysis and design, *Acta Astronaut.* 69 (9) (2011) 848–859.
- [8] L.T. DeLuca, F. Bernelli, F. Maggi, P. Tadini, C. Pardini, L. Anselmo, M. Grassi, D. Pavarin, A. Francesconi, F. Branz, Active space debris removal by a hybrid propulsion module, *Acta Astronaut.* 91 (2013) 20–33.
- [9] X. Cyril, S.W. Kim, M. Ingham, A.K. Misra, G.J. Jaar, Post-impact dynamics of two multi-body systems attempting docking/berthing, *Acta Astronaut.* 40 (11) (1997) 759–769.
- [10] D.Q. Zhou, R. Cao, Zhao Y, Micro-vibration environment measuring and analysis in remote sensing satellites (in Chinese), *Spacecraft Environ. Eng.* (6) (2013) 627–630.
- [11] X. Cyril, A.K. Misra, M. Ingham, G.J. Jaar, Postcapture dynamics of a spacecraft-manipulator-payload system, *J. Guid. Control Dyn.* 23 (1) (2000) 95–100.
- [12] C.C. Liu, X.J. Jing, S. Daley, F.M. Li, Recent advances in micro-vibration isolation, *Mech. Syst. Signal Process.* 56 (2015) 55–80.
- [13] W.H. Park, Mass-spring-damper response to repetitive impact, *J. Eng. Indus.* 89 (4) (1967) 587–596.
- [14] A. Carrella, M.J. Brennan, T.P. Waters, Static analysis of a passive vibration isolator with quasi-zero-stiffness characteristic, *J. Sound Vib.* 301 (3) (2007) 678–689.
- [15] A. Carrella, M.J. Brennan, I. Kovacic, T.P. Waters, On the force transmissibility of a vibration isolator with quasi-zero-stiffness, *J. Sound Vib.* 322 (4) (2009) 707–717.
- [16] W.S. Robertson, M.R. Kidner, B.S. Cazzolato, A.C. Zander, Theoretical design parameters for a quasi-zero stiffness magnetic spring for vibration isolation, *J. Sound Vib.* 26 (1) (2009) 88–103.
- [17] D.L. Xu, Q.P. Yu, J.X. Zhou, S.R. Bishop, Theoretical and experimental analyses of a nonlinear magnetic vibration isolator with quasi-zero-stiffness characteristic, *J. Sound Vib.* 332 (14) (2013) 3377–3389.
- [18] X.T. Sun, J. Xu, X.J. Jing, L. Cheng, Beneficial performance of a quasi-zero-stiffness vibration isolator with time-delayed active control, *Int. J. Mech. Sci.* 82 (2014) 32–40.
- [19] Y.S. Zheng, X. Zhang, Y.J. Luo, B. Yan, C.C. Ma, Design and experiment of a high-static-low-dynamic stiffness isolator using a negative stiffness magnetic spring, *J. Sound Vib.* 360 (2016) 31–52.
- [20] G.X. Dong, X.N. Zhang, S.L. Xie, B. Yan, Y.J. Luo, Simulated and experimental studies on a high-static-low-dynamic stiffness isolator using magnetic negative stiffness spring, *Mech. Syst. Signal Process.* 86 (2017) 188–203.
- [21] Y.S. Zheng, X. Zhang, Y.J. Luo, Y.H. Zhang, S.L. Xie, Analytical study of a quasi-zero stiffness coupling using a torsion magnetic spring with negative stiffness, *Mech. Syst. Signal Process.* 100 (2018) 135–151.
- [22] Q.J. Cao, Y.W. Han, T.W. Liang, M. Wiercigroch, S. Piskarev, Multiple buckling and codimension-three bifurcation phenomena of a nonlinear oscillator, *Int. J. Bifurcat. Chaos* 24 (01) (2014) 1430005.
- [23] H.H. Dai, X.C. Wang, M. Schnoor, S.N. Atluri, Analysis of internal resonance in a two-degree-of-freedom nonlinear dynamical system, *Commun. Nonlinear Sci. Numer. Simul.* 49 (2017) 176–191.
- [24] R.L. Tian, Q.J. Cao, Z.X. Li, Hopf bifurcations for the recently proposed smooth-and-discontinuous oscillator, *Chin. Phys. Lett.* 27 (7) (2010) 074701.
- [25] D. Thayer, M. Campbell, J. Vagners, A. von Flotow, Six-axis vibration isolation system using soft actuators and multiple sensors, *J. Spacecraft Rockets* 39 (2) (2002) 206–212.
- [26] E.H. Anderson, J.P. Fumo, R.S. Erwin, Satellite ultraquiet isolation technology experiment (suite), 2000 IEEE Aerospace Conference Proceedings, vol. 4, IEEE, 2000, pp. 299–313.
- [27] C.S. Wei, J.J. Luo, H.H. Dai, Z.Y. Yin, W.H. Ma, J.P. Yuan, Globally robust explicit model predictive control of constrained systems exploiting SVM-based approximation, *Int. J. Robust Nonlinear Control* 27 (16) (2016) 3000–3027.
- [28] C.S. Wei, J.J. Luo, H.H. Dai, J.P. Yuan, J.F. Xie, Efficient adaptive constrained control with time-varying predefined performance for a hypersonic flight vehicle, *Int. J. Adv. Rob. Syst.* 14 (2) (2017) 1–7.
- [29] C.S. Wei, J.J. Luo, H.H. Dai, Z.Y. Yin, J.P. Yuan, Low-complexity differentiator-based decentralized fault-tolerant control of uncertain large-scale nonlinear systems with unknown dead zone, *Nonlinear Dyn.* 89 (4) (2017) 2573–2592.
- [30] H.P. Gavin, R.D. Hanson, F.E. Filisko, Electrorheological dampers, part i: analysis and design, *J. Appl. Mech.* 63 (3) (1996) 669–675.
- [31] H.U. Oh, Characteristics of a magneto-rheological fluid isolator obtained by permanent magnet arrangements, *Smart Mater. Struct.* 13 (3) (2004) N29.
- [32] W.W. Clark, Vibration control with state-switched piezoelectric materials, *J. Intell. Mater. Syst. Struct.* 11 (4) (2000) 263–271.
- [33] X.T. Sun, X.J. Jing, J. Xu, L. Cheng, Vibration isolation via a scissor-like structured platform, *J. Sound Vib.* 333 (9) (2014) 2404–2420.
- [34] X.T. Sun, X.J. Jing, A nonlinear vibration isolator achieving high-static-low-dynamic stiffness and tunable anti-resonance frequency band, *Mech. Syst. Signal Process.* 80 (2016) 166–188.
- [35] Z.J. Wu, X.J. Jing, J. Bian, F.M. Li, R. Allen, Vibration isolation by exploring bio-inspired structural nonlinearity, *Bioinspiration Biomimetics* 10 (5) (2015) 056015.
- [36] C.C. Liu, X.J. Jing, F.M. Li, Vibration isolation using a hybrid lever-type isolation system with an x-shape supporting structure, *Int. J. Mech. Sci.* 98 (2015) 169–177.
- [37] X.T. Sun, X.J. Jing, Analysis and design of a nonlinear stiffness and damping system with a scissor-like structure, *Mech. Syst. Signal Process.* 66 (2016) 723–742.

- [38] Z.J. Wu, X.J. Jing, B. Sun, F.M. Li, A 6DOF passive vibration isolator using x-shape supporting structures, *J. Sound Vib.* 380 (2016) 90–111.
- [39] R. Pfeifer, M. Lungarella, F. Iida, Self-organization, embodiment, and biologically inspired robotics, *Science* 318 (5853) (2007) 1088–1093.
- [40] L. Liu, E.H. Dowell, J.P. Thomas, A high dimensional harmonic balance approach for an aeroelastic airfoil with cubic restoring forces, *J. Fluids Struct.* 23 (7) (2007) 351–363.
- [41] H.H. Dai, X.K. Yue, J.P. Yuan, D. Xie, A fast harmonic balance technique for periodic oscillations of an aeroelastic airfoil, *J. Fluids Struct.* 50 (2014) 231–252.
- [42] C.S. Liu, H.H. Dai, S. N Atluri, A further study on using $\dot{\mathbf{x}} = \lambda[\alpha\mathbf{R} + \beta\mathbf{P}]$ ($\mathbf{P} = \mathbf{F} - \mathbf{R}(\mathbf{F} \cdot \mathbf{R})/\|\mathbf{R}\|^2$) and $\dot{\mathbf{x}} = \lambda[\alpha\mathbf{F} + \beta\mathbf{P}^*]$ ($\mathbf{P}^* = \mathbf{R} - \mathbf{F}(\mathbf{F} \cdot \mathbf{R})/\|\mathbf{F}\|^2$) in iteratively solving the nonlinear system of algebraic equations $\mathbf{F}(\mathbf{x}) = \mathbf{0}$, *Comput. Model. Eng. Sci.* 81 (2) (2011) 195–227.